

Ground Vehicle Navigation in GNSS-Challenged Environments Using Signals of Opportunity and a Closed-Loop Map-Matching Approach

Mahdi Maaref^{ID} and Zaher M. Kassas^{ID}, *Senior Member, IEEE*

Abstract—A ground vehicle navigation approach in a global navigation satellite system (GNSS)-challenged environments is developed, which uses signals of opportunity (SOPs) in a closed-loop map-matching fashion. The proposed navigation approach employs a particle filter that estimates the ground vehicle's state by fusing pseudoranges drawn from ambient SOP transmitters with road data stored in commercial maps. The problem considered assumes the ground vehicle to have *a priori* knowledge about its initial states as well as the position of SOPs. The proposed closed-loop approach estimates the vehicle's states for subsequent time as it navigates without the GNSS signals. In this approach, a particle filter is employed to continuously estimate the vehicle's position and velocity along with the clock error states of the vehicle-mounted receiver and SOP transmitters. The simulation and experimental results with cellular long-term evolution (LTE) SOPs are presented, evaluating the efficacy and accuracy of the proposed framework in different driving environments. The experimental results demonstrate a position root-mean-squared error (RMSE) of: 1.6 m over a 825-m trajectory in an urban environment with five cellular LTE SOPs, 3.9 m over a 1.5-km trajectory in a suburban environment with two cellular LTE SOPs, and 3.6 m over a 345-m trajectory in a challenging urban environment with two cellular LTE SOPs. It is demonstrated that incorporating the proposed map-matching algorithm reduced the position RMSE by 74.88%, 58.15%, and 46.18% in these three environments, respectively, from the RMSE obtained by an LTE-only navigation solution.

Index Terms—Signals of opportunity, autonomous ground vehicle, map-matching, particle filter.

I. INTRODUCTION

AUTONOMOUS ground vehicles (AGVs), also known as self-driving cars, promise to bring an economic and a transportation revolution and to improve the quality of life. AGVs are predicted to annually prevent 5M accidents and 2M injuries, conserve 7B liters of fuel, and save 30K lives and \$190B in healthcare costs associated with accidents in the U.S. [1]. As ground vehicles progress towards fully autonomy, they will demand an extremely reliable and accurate

navigation system [2], [3]. Today's car navigation systems fuse multi-modal information from global navigation satellite systems (GNSS) receivers, vehicle motion and proximity sensors, vehicle kinematic models, and digital maps [4]. GNSS receivers are used to aid onboard dead-reckoning (DR)-type sensors (e.g., inertial navigation system (INS) and lidar) and to provide a navigation solution in a global frame, which gets matched to the digital map [5]–[8]. Map-matching is the process of associating the vehicle's navigation solution with a spatial road map [9], [10]. Map-matching algorithms enhance the navigation solution by incorporating precise road network data and *a priori* information of road features [11]. Map suppliers have dedicated considerable attention recently to develop highly accurate digital maps to meet the requirements of AGVs [12].

On-line and off-line map-matching approaches match the vehicle's position estimate, produced by GNSS receivers and onboard DR sensors, with the digital road map. However, current navigation systems will not meet the stringent reliability and accuracy demands of AGVs, due to their heavy reliance on GNSS signals. These signals get severely attenuated in urban environments and are susceptible to unintentional and intentional interference (i.e., jamming) and malicious spoofing [13]–[15]. Without GNSS signals, errors in DR sensors accumulate, compromising the safe and efficient operation of the AGV.

Recently, signals of opportunity (SOPs) have been used to overcome GNSS drawbacks [16]–[19]. Recent research have demonstrated how to exploit SOPs (e.g., cellular signals [20]–[23], digital television signals [24], [25], AM/FM signals [26], [27], and low Earth orbit satellite signals [28], [29]) to produce a navigation solution in a standalone fashion and in an integrated fashion, aiding INS and lidar [30]–[33]. SOPs are abundant and are free to use. Moreover, cellular SOPs, in particular, inherently possess desirable characteristics for navigation purposes: (i) ubiquity, (ii) high received power, (iii) large transmission bandwidth, (iv) wide range of transmission frequencies, and (v) geometric diversity [34].

This paper considers the following practical scenario. A ground vehicle is equipped with a GNSS receiver and a separate receiver capable of producing pseudoranges to ambient SOP transmitters. When the vehicle enters a GNSS-challenged environments (e.g., a deep urban canyon or an environment under a malicious jamming attack on the GNSS frequency

Manuscript received April 28, 2018; revised December 10, 2018 and February 22, 2019; accepted March 11, 2019. Date of publication June 13, 2019; date of current version June 29, 2020. This work was supported in part by the National Science Foundation (NSF) under Grant 1566240 and in part by the Office of Naval Research (ONR) under Grant N00014-16-1-2809. The Associate Editor for this paper was B. Seibold. (*Corresponding author: Zaher M. Kassas.*)

The authors are with the Department of Mechanical & Aerospace Engineering and the Department of Electrical Engineering & Computer Science, University of California, Irvine, CA 92697 USA (e-mail: mmaaref@ucr.edu; zkassas@ieee.org).

Digital Object Identifier 10.1109/TITS.2019.2907851

1524-9050 © 2019 IEEE. Personal use is permitted, but republication/redistribution requires IEEE permission.
See <https://www.ieee.org/publications/rights/index.html> for more information.

band), GNSS signals are no longer usable or reliable. In the absence of GNSS measurements, the accumulated errors of DR-type sensors grow unboundedly. However, SOPs can be used as an aiding source to bound the navigation errors [30], [33]. Exploiting ambient SOPs in the environment alleviates the need for costly, bulky, and computationally intensive sensors (e.g., INS, lidar, and camera). Nevertheless, if the vehicle is equipped with such sensors and/or if GNSS signals are available, the proposed framework could seamlessly integrate the outputs of these sensors to improve the vehicle's navigation solution.

This paper proposes a framework for producing a ground vehicle navigation via a closed-loop map-matching algorithm. The proposed framework operates in two modes: Mode 1 triggers when GNSS signals are available and fuses the GNSS-derived estimates, SOP pseudorange measurements, and the digital road map and Mode 2 triggers when GNSS signals are unavailable or unusable and fuses SOP pseudorange measurements and the digital road map. In Mode 2, the proposed framework assumes the vehicle (i) to have *initial* knowledge of its own states (e.g., from its navigation system just before GNSS signals became unavailable) and (ii) to be equipped with: (i) a receiver capable of producing pseudorange measurements to ambient SOPs (e.g., [22], [25], [35], [36]) and (ii) a digital map of the road segments and SOP locations.

This paper makes two contributions. First, a novel closed-loop map-matching framework for navigation in both GNSS-available and GNSS-challenged environments is developed. The framework simultaneously estimates the vehicle's position and velocity states along with the difference between the vehicle-mounted receiver's dynamic stochastic clock error states (bias and drift) and the clock error states of each SOP clock. A computationally efficient particle filter that fuses digital map data and SOP pseudoranges is adopted. Second, the accuracy and efficacy of the proposed framework is analyzed through four simulation and three experimental tests. The experimental tests used real cellular long-term evolution (LTE) SOPs and were conducted on a ground vehicle in different environments, including (i) an urban environment where multipath severely affected the received LTE signals, (ii) a suburban environment where LTE SOPs had a poor geometric diversity and the vehicle had limited line-of-sight (LOS) to LTE towers, and (iii) a GNSS-challenged urban environment with multiple junctions and GNSS cutoff conditions, while using pseudorange measurements from only 2 LTE SOPs. The experimental results in these three environment show respectively a (i) position root-mean squared error (RMSE) of 1.6 m over a 825 m trajectory in the urban environment with 5 LTE SOPs, (ii) position RMSE of 3.9 m over a 1.5 km trajectory in the suburban environment with 2 LTE SOPs, and (iii) position RMSE of 3.6 m over a 345 m trajectory in the challenging urban environment with 2 LTE SOPs. Moreover, it is demonstrated that incorporating the proposed map-matching algorithm reduced the position RMSE by 74.88% and 58.15% in urban and suburban environments, respectively, from the RMSE obtained by an LTE-only navigation.

The remainder of this paper is organized as follows. Section II surveys related research on map-matching strategies

for ground vehicle navigation and highlights the difference between existing approaches and the proposed approach. Section III describes the vehicle and SOP dynamic models, the SOP pseudorange measurement model, and the digital map model. Section IV develops the map-matching framework that fuses the digital map with SOP pseudorange measurements. Sections V and VI present simulation and experimental results, respectively, evaluating the performance of the proposed framework. Concluding remarks and future work are given in Section VII.

II. RELATED WORK

Map-matching for ground vehicle navigation has been studied in the literature. In [9], a map-matching framework was proposed that provided integrity provision at the lane-level. The framework defined the integrity as the capability of the system to detect performance anomalies and warn the user whenever the system should not be used. The proposed method fused measurements from a GNSS receiver, an odometer, and a gyroscope with road information through a multiple-hypothesis particle filter. In [37], three factors of currently used algorithms in floating car data (FCD) were discussed: distance, speed-direction, and connectivity. The characteristics of highway networks were analyzed, and a map-matching approach was proposed based on the gradual-removal of candidate roads. In [38], a ground vehicle navigation framework was proposed that performs map-matching by adaptively choosing the appropriate timing and matching method according to the complexity of the local network to which the positioning point belongs. This method is experimentally shown to be beneficial due to the fact that using fixed time interval can result in a lack of efficiency and accuracy if the initial point is not correctly matched. In [39], a cooperative map-matching approach for vehicle positioning was introduced, which established a vehicle-to-vehicle (V2V) communication approach in a vehicular ad hoc network (VANET) to exchange GNSS-derived information between vehicles. In [40], a method for accurate and efficient map-matching for challenging environments was presented. This method considered a number of heuristics rooted in a set of observations from real-life usage scenarios (e.g., traffic distribution on different roads). The framework used the cellular location information and was shown to be able to achieve better results compared to traditional hidden Markov model (HMM)-based map-matching frameworks, in cases where the cellular-derived localization error was on the order of kilometers. In [11], a map-matching approach was proposed that uses an HMM tailored for noisy and sparse data to generate partial map-matched paths in an online manner. In [41], a particle filter was employed to fuse the magnetometer data with the digital map to estimate the vehicle's position and heading. In [42], a framework was presented that used a multiple-hypothesis algorithm for fusing the navigation solution of a global positioning system (GPS)-INS system with digital maps. The framework included an algorithm to evaluate whether the map-matched results could be used to calibrate the sensors in order to increase the positioning accuracy. Since the number of hypothesis nodes in map-matching algorithms

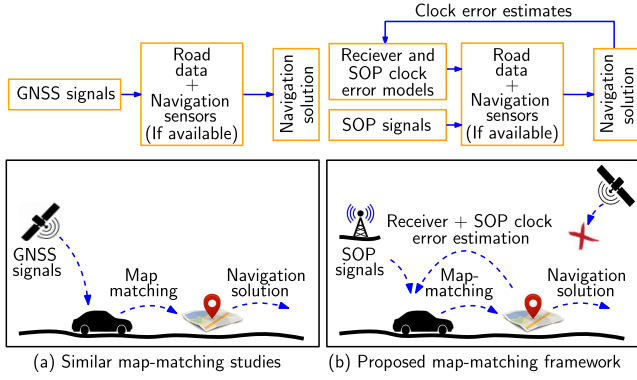


Fig. 1. Comparison between the proposed framework and existing map-matching approaches. (a) Existing map-matching approaches assume the availability of GNSS signals, which are fused with road data to refine the vehicle’s navigation solution. (b) The proposed approach operates in the absence of GNSS signals. Here, SOPs are fused with road data to refine the vehicle’s navigation solution. The navigation solution is fed back to refine the estimates of the receiver’s and SOPs’ clock error states.

grows exponentially with time, the framework proposed a strategy to reduce the number of hypotheses by pruning the branches of the multiple-hypothesis tree and eliminating and merging the redundant nodes. In [43], reusability of historical information was evaluated along with spatial-temporal patterns in the arrangement of the projected GNSS points to the road networks. To this end, a machine learning framework was developed that detected and validated the spatial-temporal patterns in projection vectors produced by map-matching. The problem of using the digital map data to correct the sensor error has been also studied in the literature [44]–[46]. Due to the fact that the errors in digital maps is typically smaller than sensor error, the digital map information can be used to correct the accumulated error in DR-type sensors (e.g., INS) [42].

In contrast to existing map-matching approaches, to the author’s knowledge, this is the first paper that develops a map-matching approach for SOP-derived estimates, while dealing with the problem of unknown clock error states of the SOP transmitters. Unlike GNSS-based navigation where the clock error states of GNSS satellites are known by decoding the navigation message, the complexity with SOPs is that their clock error states are unknown and must be estimated. In this paper, a closed-loop map-matching approach is developed, where the refined vehicle position estimate obtained from fusing SOP pseudoranges and digital road maps is used in a feedback to refine estimates of the clock error states. Fig. 1 compares the existing GNSS-based map-matching approaches with the proposed closed-loop SOP-based map-matching framework. In the GNSS-based approaches (e.g., [10]) the algorithm is open-loop with inputs being GNSS signals, digital maps, and navigation sensors (if any) and the output being the refined navigation solution. In the proposed method, however, the algorithm is closed-loop where the navigation solution is fed back to refine estimates of the receiver and SOPs clock error states.

III. MODEL DESCRIPTION

This section describes the dynamic model of the vehicle, SOP transmitters [47], [48], and geographical digital maps.

Also, it specifies the pseudorange measurement model made by the vehicle-mounted receiver on SOP transmitters.

A. Vehicle and SOP Dynamics Model

The navigation environment is assumed to comprise N_s terrestrial SOP transmitters, denoted $\{S_n\}_{n=1}^{N_s}$. It is assumed that the vehicle knows the location of the SOP transmitters (e.g., from a local or a cloud-hosted database). In practice, one could map the SOP transmitter locations *a priori* via several approaches, such as radio mapping or satellite images and store them in a database, which is continuously maintained. This has been the subject of prior research (e.g., [25], [48], [49]). In this paper, LTE cellular SOPs were used to experimentally evaluate the performance of the proposed approach, as discussed in Section VI. This was due to the availability of an LTE receiver that provided pseudorange measurements. However, the proposed framework is agnostic to the type of SOP and could accommodate other SOP types (e.g., cellular CDMA, digital television, AM/FM radio) from which pseudorange measurements are extracted via appropriate receivers.

Each SOP tower is assumed to be spatially stationary. Although the SOP locations are assumed to be known, their clock error states (i.e., clock bias and drift) are unknown, dynamic, and stochastic; hence, they must be estimated continuously. The dynamics of the clock bias and drift is typically modeled as a double-integrator driven by a process noise [50]–[53]. This model is valid over a relatively short periods of time for both the SOP transmitters and the vehicle-mounted receiver. Since the SOP pseudorange measurement is parameterized by the difference between the receiver’s and the SOP’s clock biases [47], one only needs to estimate the difference in clock biases and clock drifts, reducing the number of clock error states that need to be estimated from $2N_s + 2$ to $2N_s$. Hence, each SOP will be associated with a state vector $\Delta \mathbf{x}_{\text{clk},s_n}$ that consists of the difference between its clock bias and drift with the clock bias and drift of the vehicle-mounted receiver, i.e.,

$$\Delta \mathbf{x}_{\text{clk},s_n} \triangleq [c \Delta \delta t_n, c \Delta \dot{\delta} t_n]^T, \quad n = 1, \dots, N_s,$$

where c is the speed of light, $\Delta \delta t_n = \delta t_r - \delta t_{s_n}$ is the difference between the receiver’s clock bias δt_r and the n -th SOP’s clock bias δt_{s_n} , and $\Delta \dot{\delta} t_n = \dot{\delta} t_r - \dot{\delta} t_{s_n}$ is the difference between the receiver’s clock drift $\dot{\delta} t_r$ and the n -th SOP’s clock drift $\dot{\delta} t_{s_n}$.

Accordingly, the discrete-time dynamic model of the clock error states can be expressed as

$$\Delta \mathbf{x}_{\text{clk}}(k+1) = \Phi_{\text{clk}} \Delta \mathbf{x}_{\text{clk}}(k) + \mathbf{w}_{\text{clk}}(k), \quad (1)$$

$$\Phi_{\text{clk}} \triangleq \begin{bmatrix} \mathbf{F}_{\text{clk}} & \mathbf{0} & \dots & \mathbf{0} \\ \mathbf{0} & \mathbf{F}_{\text{clk}} & \dots & \mathbf{0} \\ \vdots & \vdots & \ddots & \vdots \\ \mathbf{0} & \mathbf{0} & \dots & \mathbf{F}_{\text{clk}} \end{bmatrix}, \quad \mathbf{F}_{\text{clk}} \triangleq \begin{bmatrix} 1 & T \\ 0 & 1 \end{bmatrix},$$

where $\Delta \mathbf{x}_{\text{clk}} = [\Delta \mathbf{x}_{\text{clk},s_1}^T, \dots, \Delta \mathbf{x}_{\text{clk},s_{N_s}}^T]^T$, T is the sampling time, and \mathbf{w}_{clk} is the process noise, which is modeled as a discrete-time zero-mean white random sequence with covariance

$$\mathbf{Q}_{\text{clk}} = \Gamma \mathbf{Q}_{\text{clk},r,s} \Gamma^T, \quad (2)$$

where

$$\Gamma \triangleq \begin{bmatrix} \mathbf{I}_{2 \times 2} & -\mathbf{I}_{2 \times 2} & \mathbf{0} & \dots & \mathbf{0} \\ \mathbf{I}_{2 \times 2} & \mathbf{0} & -\mathbf{I}_{2 \times 2} & \dots & \mathbf{0} \\ \vdots & \vdots & \vdots & \ddots & \vdots \\ \mathbf{I}_{2 \times 2} & \mathbf{0} & \mathbf{0} & \dots & -\mathbf{I}_{2 \times 2} \end{bmatrix},$$

and $\mathbf{Q}_{\text{clk},r,s} \triangleq \text{diag}[\mathbf{Q}_{\text{clk},r}, \mathbf{Q}_{\text{clk},s_1}, \dots, \mathbf{Q}_{\text{clk},s_{N_s}}]$. Here, $\mathbf{Q}_{\text{clk},s_n}$ is the process noise covariance of the n -th SOP, which is given by

$$\mathbf{Q}_{\text{clk},s_n} = c^2 \begin{bmatrix} S_{\tilde{w}_{\delta t,s_n}} T + S_{\tilde{w}_{\delta t,s_n}} \frac{T^3}{3} & S_{\tilde{w}_{\delta t,s_n}} \frac{T^2}{2} \\ S_{\tilde{w}_{\delta t,s_n}} \frac{T^2}{2} & S_{\tilde{w}_{\delta t,s_n}} T \end{bmatrix},$$

where $S_{\tilde{w}_{\delta t,s_n}}$ and $S_{\tilde{w}_{\delta t,s_n}}$ are the power spectra of the continuous-time process noise $\tilde{w}_{\delta t,s_n}$ and $\tilde{w}_{\delta t,s_n}$, driving the clock bias and clock drift, respectively [48], [53]. Note that $\mathbf{Q}_{\text{clk},r}$ has the same form as $\mathbf{Q}_{\text{clk},s_n}$, except that $S_{\tilde{w}_{\delta t,s_n}}$ and $S_{\tilde{w}_{\delta t,s_n}}$ are replaced by the receiver-specific spectra $S_{\tilde{w}_{\delta t,r}}$ and $S_{\tilde{w}_{\delta t,r}}$, respectively. The spectra $S_{\tilde{w}_{\delta t,r}}$ and $S_{\tilde{w}_{\delta t,s_n}}$ can be related to the power-law coefficients, $\{h_\alpha\}_{\alpha=-2}$, which have been shown through laboratory experiments to characterize the power spectral density of the fractional frequency deviation $y(f)$ of an oscillator from nominal frequency, namely, $S_y(f) = \sum_{\alpha=-2}^2 h_\alpha f^\alpha$ [50], [53]. It is common to approximate such relationship by considering only the frequency random-walk coefficient h_{-2} and the white frequency coefficient h_0 , which lead to $S_{\tilde{w}_{\delta t,r}} \approx \frac{h_0}{2}$ and $S_{\tilde{w}_{\delta t,s_n}} \approx 2\pi^2 h_{-2}$ [51], [52].

The vehicle's state vector \mathbf{x}_r consists of the vehicle's two-dimensional (2-D) position $\mathbf{p}_r = [p_{r,x}, p_{r,y}]^\top$ and velocity \mathbf{v}_r , i.e., $\mathbf{x}_r \triangleq [\mathbf{p}_r^\top, \mathbf{v}_r^\top]^\top$, expressed in the global frame \mathcal{G} (Latitude-Longitude coordinates). The vehicle is assumed to be moving according to velocity random walk dynamics, which can be expressed in discrete-time by

$$\mathbf{x}_r(k+1) = \mathbf{A}_r \mathbf{x}_r(k) + \mathbf{w}_r(k), \quad (3)$$

$$\mathbf{A}_r = \begin{bmatrix} \mathbf{I}_{2 \times 2} & T \mathbf{I}_{2 \times 2} \\ \mathbf{0}_{2 \times 2} & \mathbf{I}_{2 \times 2} \end{bmatrix},$$

where \mathbf{w}_r is a discrete-time zero-mean white noise sequence with covariance \mathbf{Q}_r given by

$$\mathbf{Q}_r = \begin{bmatrix} \tilde{q}_x \frac{T^3}{3} & 0 & \tilde{q}_x \frac{T^2}{2} & 0 \\ 0 & \tilde{q}_y \frac{T^3}{3} & 0 & \tilde{q}_y \frac{T^2}{2} \\ \tilde{q}_x \frac{T^2}{2} & 0 & \tilde{q}_x T & 0 \\ 0 & \tilde{q}_y \frac{T^2}{2} & 0 & \tilde{q}_y T \end{bmatrix},$$

where \tilde{q}_x and \tilde{q}_y are the power spectral densities of the continuous-time process noise $\tilde{\mathbf{w}}_r$, driving the acceleration in x - and y -directions, respectively. The velocity random walk motion model is general enough to account for a wide range of moving objects, while being mathematically tractable.

B. Map Model

Digital maps provide geographical data and location information, which can be used for aligning noisy traces and displaying traversed trajectories. Digital maps are extensively used in modern navigation systems for accurate vehicle guidance and advanced driver-assistance systems (ADAS) functions. To this end, geographical information systems (GISs),

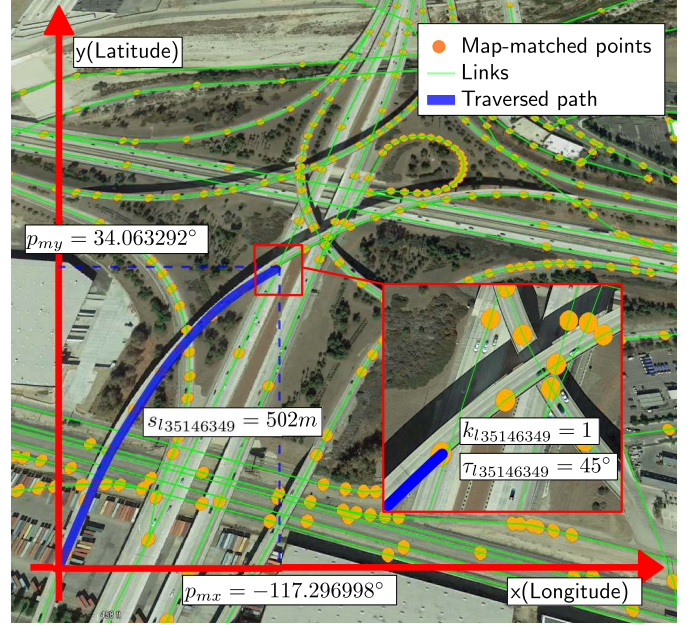


Fig. 2. An example digital map and its corresponding map-matched points and links.

which represent the roads as series of links, are employed with map-matching techniques to snap the recorded vehicle trajectory trace (e.g., from a GNSS navigation solution) to the digital road map. Each link includes the driving road centerline coordinates, the lane information, and the road heading angle [9], [54]. A set of map-matched positions for a sample link of a map with unique link identifier l are defined based on k_{l_n} , s_{l_n} , and τ_{l_n} , where $k_{l_n} \in \mathbb{N}$ is the lane identifier, $s_{l_n} \in \mathbb{R}$ is the offset from the first map-matched position in link l , and τ_{l_n} is the heading angle. The link l is assumed to comprise L_N map-matched positions, denoted $\{\mathbf{l}_n\}_{n=1}^{L_N}$. It can be shown that for any link l , there exist two recursive functions \mathcal{M}_l and \mathcal{N}_l that return the 2-D position vector of the n -th map-matched position $\mathbf{p}_m \triangleq [p_{m,x}, p_{m,y}]^\top$, expressed in the global frame \mathcal{G} (see Appendix A), specifically

$$p_{m,x_n} = \mathcal{M}_l(p_{m,x_{n-1}}, s_{l_n}, s_{l_{n-1}}, \tau_{l_{n-1}}, k_{l_n}), \quad (4)$$

$$p_{m,y_n} = \mathcal{N}_l(p_{m,y_{n-1}}, s_{l_n}, s_{l_{n-1}}, \tau_{l_{n-1}}, k_{l_n}),$$

where $p_{m,x} \in \{p_{m,x_n}\}_{n=1}^{L_N}$ and $p_{m,y} \in \{p_{m,y_n}\}_{n=1}^{L_N}$ represent the 2-D map-matched vehicle position. Fig. 2 shows an example of a digital map including the links and map-matched positions, which are superimposed on a Google Map.

The map used in this study is developed based on an Open Street Map (OSM) database [55] for Riverside, California. OSM is built by a community of mappers that contribute and maintain roads, trails, and railway stations information. A MATLAB-based parser was developed to extract the road coordinates and lane information and interpolate map-matched positions between two successive points with a distance greater than a specified threshold. Fig. 2 shows the interchange road junction between interstate highways 215 and 10 in Riverside, California. This area contains 131 links and 2,441 map-matched positions, which are presented with green lines

and brown circles, respectively. The lane identifier and link offset for the 35,146,349-th link of the OSM database and its corresponding map-matched positions are illustrated.

Some approaches in the literature consider the maps to be faultless (e.g., [56], [57]); however, in the proposed approach, the map displacement error \mathbf{w}_m is modeled as a zero-mean random vector with covariance $\Sigma_m = \text{diag}[\sigma^2_{m_x}, \sigma^2_{m_y}]$. To find the map-matched vehicle's position at time-step k , while accounting for the map displacement error, the proposed model finds the closest Mahalanobis distance on the map to the estimated vehicle's position at time-step k . The Mahalanobis distance provides a powerful method of measuring how similar some set of observations is to an ideal set of observations with some known mean and covariance. The estimated position and map-matched position of the vehicle at time-step k are assumed to be $\hat{\mathbf{p}}_r(k)$ and $\hat{\mathbf{p}}_m(k)$, respectively. Subsequently

$$\hat{\mathbf{p}}_m(k) = \min_{l_n} \|\hat{\mathbf{p}}_r(k) - \mathbf{l}_n\|_{\Sigma_m}, \quad (5)$$

where

$$\|\hat{\mathbf{p}}_r(k) - \mathbf{l}_n\|_{\Sigma_m} = \sqrt{[\hat{\mathbf{p}}_r(k) - \mathbf{l}_n]^T \Sigma_m^{-1} [\hat{\mathbf{p}}_r(k) - \mathbf{l}_n]}.$$

Note that $\hat{\mathbf{p}}_r(k)$ will be defined later in Subsection IV-C.

C. Pseudorange Observation Model

After discretization and mild approximations, the pseudorange made by the vehicle-mounted receiver on the n -th SOP is given by [47]

$$z_{s_n}(k) = \|\mathbf{p}_r(k) - \mathbf{p}_{s_n}\|_2 + c\Delta\delta t_n(k) + w_{s_n}, \quad (6)$$

where \mathbf{p}_{s_n} is the location of the n -th SOP tower and w_{s_n} is the measurement noise, which is modeled as a discrete-time zero-mean white Gaussian sequence with variance $\sigma_{s_n}^2$. The vector of pseudorange measurements to all N_s SOPs is given by

$$\mathbf{z}_s = [z_{s_1}, \dots, z_{s_{N_s}}]^T, \quad (7)$$

and it is assumed that the measurement noise $\{w_{s_n}\}_{n=1}^{N_s}$ are independent.

IV. CLOSED-LOOP MAP-MATCHING FRAMEWORK FOR VEHICLE STATE ESTIMATION USING SOPs

This section describes a closed-loop framework to map-match the vehicle's position estimate using SOP pseudoranges.

A. Problem Formulation

A vehicle with velocity random walk dynamics (cf. (3)) is assumed to navigate in an environment comprising N_s SOP transmitters. The location of these transmitters are assumed to be known. In Mode 1, GNSS signals are available and GNSS-derived vehicle position-estimates are map-matched to the road map. In Mode 2, GNSS signals become unavailable and the proposed framework:

- uses the last map-matched, GNSS-derived estimates for initialization,

- uses SOP pseudoranges to estimate the vehicle's position and velocity and map-matches the position estimate with the road network data, and
- continuously estimates the clock error states of the vehicle-mounted receiver and SOP transmitters.

A particle filter is adapted for data fusion, which simultaneously performs both position refinement and clock error estimation. Particle filters are relatively easy to implement [58] and provide a probabilistic framework for fusing digital map data and non-linear, non-Gaussian measurements. Finally, particle filters could track multiple candidate road segments, which helps recover from mismatches.

B. Time Update

In this subsection, the particle filter time update step for both modes is described. The i -th particle vector is defined as

$$\mathcal{X}^i(k) \triangleq [\mathcal{P}_r^i(k), \mathcal{V}_r^i(k), \mathcal{D}\mathbf{x}_{\text{clk}}^i(k)]^T,$$

where $\mathcal{P}_r^i(k)$, $\mathcal{V}_r^i(k)$, and $\mathcal{D}\mathbf{x}_{\text{clk}}^i(k)$ represent the i -th particle position, velocity, and clock error state, respectively, at time-step k . Note that

$$\begin{aligned} \mathcal{D}\mathbf{x}_{\text{clk}}^i &\triangleq [\mathcal{D}\mathbf{x}_{\text{clk},1}^i, \dots, \mathcal{D}\mathbf{x}_{\text{clk},N_s}^i]^T, \\ \mathcal{D}\mathbf{x}_{\text{clk},n}^i &\triangleq [\mathcal{D}\mathbf{x}_{\text{bias},n}^i, \mathcal{D}\mathbf{x}_{\text{drift},n}^i]^T, \end{aligned}$$

where $\mathcal{D}\mathbf{x}_{\text{bias},n}^i$ and $\mathcal{D}\mathbf{x}_{\text{drift},n}^i$ represent the i -th particle of the difference between the receiver's clock bias/drift and the n -th SOP's clock bias/drift.

The first step is to draw the initial particles $\mathcal{X}^i(0)$ for $i = 1, \dots, N$ from an initial probability density $p[\mathbf{x}(0)]$, where $\mathbf{x}(0) = [\mathbf{p}_r^T(0), \mathbf{v}_r^T(0), \Delta\mathbf{x}_{\text{clk}}^T(0)]^T$, i.e.,

$$\mathcal{X}^i(0) \sim p[\mathbf{x}(0)], \quad i = 1, \dots, N.$$

The GNSS-derived estimates before GNSS cutoff is used to initialize the particles. Initially, the particle weights are assumed to be equal, i.e.,

$$\mathcal{W}^i(0) = \frac{1}{N}, \quad i = 1, \dots, N.$$

Note that the primed $\mathcal{W}^i(\cdot)$ denotes that the weights are not yet normalized. The particle filter samples sequentially from the sequence of posterior probability density $p[\mathbf{x}(k)|\mathbf{z}_s(k)]$. It can be shown that in order to minimize the variance of the weights at time-step k , the prior $p[\mathbf{x}(k)|\mathbf{x}(k-1)]$ must be chosen as the importance density function $q(\cdot)$, namely [59]

$$q[\mathbf{x}(k)] = p[\mathbf{x}(k)|\mathbf{x}(k-1)].$$

The particular choice of importance density function is related to the process noise distribution. Here, for simplicity, samples of the process noise driving the vehicle's position and velocity \mathbf{w}_r^i and clock error $\mathbf{w}_{\text{clk}}^i$ will be drawn from a Gaussian distribution according to

$$\begin{aligned} \mathbf{w}_r^i(k-1) &\sim \mathcal{N}[\mathbf{0}, \mathbf{Q}_r], \quad \text{for } i = 1, \dots, N, \\ \mathbf{w}_{\text{clk}}^i(k-1) &\sim \mathcal{N}[\mathbf{0}, \mathbf{Q}_{\text{clk}}], \quad \text{for } i = 1, \dots, N, \end{aligned}$$

where $\mathcal{N}[\boldsymbol{\mu}, \mathbf{Q}]$ denotes a Gaussian distribution with mean $\boldsymbol{\mu}$ and covariance \mathbf{Q} . Using (1) and (3), the time update of the particles is computed from

$$\begin{bmatrix} \mathcal{P}_r^i(k) \\ \mathcal{V}_r^i(k) \\ \mathcal{D}\mathbf{x}_{\text{clk}}^i(k) \end{bmatrix} = \mathbf{F} \begin{bmatrix} \mathcal{P}_r^i(k-1) \\ \mathcal{V}_r^i(k-1) \\ \mathcal{D}\mathbf{x}_{\text{clk}}^i(k-1) \end{bmatrix} + \begin{bmatrix} \mathbf{w}_r^i(k-1) \\ \mathbf{w}_{\text{clk}}^i(k-1) \end{bmatrix},$$

where

$$\mathbf{F} = \begin{bmatrix} \mathbf{I}_{2 \times 2} & T\mathbf{I}_{2 \times 2} & \mathbf{0}_{2 \times 2N_s} \\ \mathbf{0}_{2 \times 2} & \mathbf{I}_{2 \times 2} & \mathbf{0}_{2 \times 2N_s} \\ \mathbf{0}_{2N_s \times 2} & \mathbf{0}_{2N_s \times 2} & \Phi_{\text{clk}} \end{bmatrix}. \quad (8)$$

C. Measurement Update

When GNSS signals are available (Mode 1), the measurement update stage corrects the propagated particles from the time update stage with (i) SOPs, (ii) digital map data, and (iii) the estimated vehicle's position obtained from the GNSS navigation solution $\hat{\mathbf{p}}_G \triangleq [\hat{p}_{G_x}, \hat{p}_{G_y}]^T$. Hence, the measurement vector $\mathcal{Z}(k)$ takes the form

$$\mathcal{Z}(k) \triangleq [z_{s_1}(k), \dots, z_{s_{N_s}}(k), \hat{\mathbf{p}}_G^T(k)]^T.$$

The error of the estimated position obtained from the GNSS navigation solution is modeled as a zero-mean Gaussian random vector with a horizontal covariance $\boldsymbol{\Sigma}_{\text{GNSS}}$. To account for the effect of multipath in urban environment navigation, $\boldsymbol{\Sigma}_{\text{GNSS}}$ consists of nominal errors (e.g., uncertainties in satellite clocks and positions, propagation delays in the ionosphere and troposphere, receiver noise, etc.) as well as multipath, i.e.,

$$\begin{aligned} \boldsymbol{\Sigma}_{\text{GNSS}} &= \boldsymbol{\Sigma}_{\text{GNSS,nom}} + \boldsymbol{\Sigma}_{\text{GNSS,mp}} \\ \boldsymbol{\Sigma}_{\text{GNSS,mp}} &\approx \sigma_{\text{GNSS,mp}}^2 \text{HDOP} \mathbf{I}_{2 \times 2}, \end{aligned}$$

where $\boldsymbol{\Sigma}_{\text{GNSS,nom}}$ is the horizontal covariance of the estimated error due to nominal errors, $\boldsymbol{\Sigma}_{\text{GNSS,mp}}$ is the horizontal covariance of the estimated error due to multipath, HDOP is the horizontal dilution of precision, and $\sigma_{\text{GNSS,mp}}^2$ is the contribution of multipath on the GNSS pseudorange measurement noise variance. Note that the proposed framework is agnostic to the multipath model, as long as the multipath model generates $\sigma_{\text{GNSS,mp}}^2$. Several multipath models have been proposed in the literature [60]–[64]. This paper, uses the multipath model presented in [63].

When GNSS signals become unavailable (Mode 2), the measurement update stage only uses (i) pseudoranges drawn from SOPs and (ii) digital map data to correct the propagated particles. Therefore, $\mathcal{Z}(k)$ only includes SOP measurements, i.e.,

$$\mathcal{Z}(k) \triangleq [z_{s_1}(k), \dots, z_{s_{N_s}}(k)]^T.$$

Given the particle weights $\mathcal{W}^i(k-1)$ and the measurement vector at time-step k , $\mathcal{Z}(k)$, the weights are updated according to

$$\mathcal{W}^i(k) = p[\mathcal{Z}(k)|\mathcal{X}^i(k)]\mathcal{W}^i(k-1), \quad i = 1, \dots, N.$$

In deep urban canyons with limited LOS conditions, the likelihood $p[\mathcal{Z}(k)|\mathcal{X}^i(k)]$ could possess very small values, leading to numerical underflow issues. To avoid such problem,

the log-likelihood measurement update is employed according to

$$\ln[\mathcal{W}'^i(k)] = \ln\{p[\mathcal{Z}(k)|\mathcal{X}^i(k)]\} + \ln[\mathcal{W}^i(k-1)]. \quad (9)$$

Recall that the pseudorange measurement noise in (6) was modeled as zero-mean independent Gaussian; therefore, (9) can be expressed as

$$\begin{aligned} \ln[\mathcal{W}'^i(k)] &= -\frac{1}{2}[\mathcal{Z}(k) - \mathcal{H}^i(k)]^T (\boldsymbol{\Sigma}_s)^{-1} [\mathcal{Z}(k) - \mathcal{H}^i(k)] \\ &\quad + \ln[\mathcal{W}^i(k-1)], \end{aligned} \quad (10)$$

where, for Mode 1

$$\begin{aligned} \mathcal{H}^i(k) &= \begin{bmatrix} \|\mathcal{P}_r^i(k) - \mathbf{p}_{s_1}\|_2 + \mathcal{D}x_{\text{bias},1}^i(k) \\ \vdots \\ \|\mathcal{P}_r^i(k) - \mathbf{p}_{s_{N_s}}\|_2 + \mathcal{D}x_{\text{bias},N_s}^i(k) \\ \mathcal{P}_r^i(k) \end{bmatrix}, \\ \boldsymbol{\Sigma}_s &= \text{diag}[\sigma_{s_1}^2, \dots, \sigma_{s_{N_s}}^2, \boldsymbol{\Sigma}_{\text{GNSS}}], \end{aligned}$$

and for Mode 2

$$\begin{aligned} \mathcal{H}^i(k) &= \begin{bmatrix} \|\mathcal{P}_r^i(k) - \mathbf{p}_{s_1}\|_2 + \mathcal{D}x_{\text{bias},1}^i(k) \\ \vdots \\ \|\mathcal{P}_r^i(k) - \mathbf{p}_{s_{N_s}}\|_2 + \mathcal{D}x_{\text{bias},N_s}^i(k) \end{bmatrix}, \\ \boldsymbol{\Sigma}_s &= \text{diag}[\sigma_{s_1}^2, \dots, \sigma_{s_{N_s}}^2]. \end{aligned}$$

For added numerical robustness, the largest weight is subtracted from each weight before taking the exponent of (10), which yields

$$\mathcal{W}''^i(k) = e^{\ln[\mathcal{W}'^i(k)] - \max_i \{\ln[\mathcal{W}'^i(k)]\}}. \quad (11)$$

The weights are normalized so that they sum to unity to preserve the fact that the set of particles represent a discrete approximation of the posterior probability density, i.e.,

$$\mathcal{W}^i(k) = \frac{\mathcal{W}''^i(k)}{\sum_{i=1}^N \mathcal{W}''^i(k)}.$$

Finally, the state estimate can be computed according to

$$\begin{aligned} \hat{\mathbf{p}}_r(k) &\approx \sum_{i=1}^N \mathcal{W}^i(k) \mathcal{P}_r^i(k), \\ \hat{\mathbf{v}}_r(k) &\approx \sum_{i=1}^N \mathcal{W}^i(k) \mathcal{V}_r^i(k), \\ \widehat{\Delta}\mathbf{x}_{\text{clk}}(k) &\approx \sum_{i=1}^N \mathcal{W}^i(k) \mathcal{D}\mathbf{x}_{\text{clk}}^i(k). \end{aligned}$$

The next step is to refine the estimate $\hat{\mathbf{p}}_r(k)$ with the digital map data according to (5). Then, the vehicle's estimated position is updated to be the nearest map-matched point, i.e.,

$$\hat{\mathbf{p}}_r'(k) \equiv \hat{\mathbf{p}}_m(k).$$

Subsequently, estimates $\hat{\mathbf{p}}_r(k)$ and $\hat{\mathbf{p}}_m(k)$ are fed back to correct the clock bias error state estimate according to

$$c \hat{\Delta} \delta t'_n(k) = c \hat{\Delta} \delta t_n(k) + \mathbf{\Delta}_{corr,n}(k), \quad (12)$$

where

$$\mathbf{\Delta}_{corr,n}(k) = G_p [\|\hat{\mathbf{p}}_m(k) - \mathbf{p}_{s_n}\|_2 - \|\hat{\mathbf{p}}_r(k) - \mathbf{p}_{s_n}\|_2],$$

where the design parameter $G_p \in (0, 1)$ is the proportional term of the control loop and is tuned to account for the effect of the measurement noise. In this paper, for $\sigma_{s_n}^2 = 10 \text{ m}^2$, G_p was set to 0.85. For higher value of measurement noise, G_p takes lower value. Finally, the covariance can be obtained from

$$\mathbf{P}(k) \approx \sum_{i=1}^N \mathcal{W}^i(k) [\mathcal{X}^i(k) - \hat{\mathbf{x}}(k)] [\mathcal{X}^i(k) - \hat{\mathbf{x}}(k)]^T,$$

where

$$\begin{aligned} \hat{\mathbf{x}}(k) &\triangleq [\hat{\mathbf{p}}_r^T(k), \hat{\mathbf{v}}_r^T(k), \widehat{\mathbf{\Delta}} \mathbf{x}'_{\text{clk}}(k)]^T, \\ \widehat{\mathbf{\Delta}} \mathbf{x}'_{\text{clk}}(k) &= \left[\widehat{\mathbf{\Delta}} \mathbf{x}'_{\text{clk},s_1}, \dots, \widehat{\mathbf{\Delta}} \mathbf{x}'_{\text{clk},s_{N_s}} \right]^T, \\ \widehat{\mathbf{\Delta}} \mathbf{x}'_{\text{clk},s_n} &\triangleq \left[c \hat{\Delta} \delta t'_n, c \hat{\Delta} \delta t_n \right]^T. \end{aligned}$$

D. Resampling

particle degeneracy and impoverishment are commonly encountered issues in particle filters. This is typically mitigated by including a resampling step before the weights become significantly uneven. In the resampling step, the particles with negligible weights are replaced by new particles in the proximity of the particles with higher weights. Several adaptive resampling criteria can be used, including the variance of the weights and the relative entropy with respect to the uniform distribution [59]. Here, a simple yet effective resampling scheme is adopted. First, an estimate of the effective number of particles \hat{N}_{eff} is computed as

$$\hat{N}_{eff} = \frac{1}{\sum_{i=1}^N [\mathcal{W}^i(k)]^2}.$$

If the effective number of particles is less than a given threshold N_{thr} , resampling is performed according to Algorithm 1.

This resampling approach essentially selects new particle weights such that the discrepancy between the particles' weights is reduced. Note that some old particles might appear more than once in the new set, whereas some might disappear completely. One problem associated with using map-matching in a closed-loop scheme is that if incorrect map-matched positions are used to correct for the clock error states, the error will very likely grow even larger. To avoid this, after each measurement, the position estimate is compared to the intersection of pseudoranges received from each SOPs. If the difference is greater than a pre-defined threshold, the resampling approach is used to reset the particles and re-estimate the states.

Fig. 3 demonstrates the different parts of the proposed navigation framework, including: time update, measurement update, and digital map update.

Algorithm 1: Particle Resampling

Input: $\mathcal{X}^i(k)$, $\mathcal{W}^i(k)$, and N_{thr}
Output: $\mathcal{X}^i_{new}(k)$ and $\mathcal{W}^i_{new}(k)$

- 1 Set $i = 1$
- 2 Calculate \hat{N}_{eff}
- 3 If $\hat{N}_{eff} < N_{thr}$,
- 4 Choose a random number η on $[0, 1]$ uniformly
- 5 Find α such that $\sum_{j=1}^{\alpha-1} \mathcal{W}^j(k) \leq \eta < \sum_{j=1}^{\alpha} \mathcal{W}^j(k)$
- 6 Set $\mathcal{X}^i_{new}(k) = \mathcal{X}^{\alpha}(k)$
- 7 Set $\mathcal{W}^i_{new}(k) = \frac{1}{N}$
- 8 If $i < N$,
- 9 Set $i = i + 1$
- 10 Go to Step 4
- 11 Else,
- 12 Delete the old set of particles
- 13 Use the new set of particles with new weights
- 14 End if
- 15 Else,
- 16 Do not resample
- 17 End if

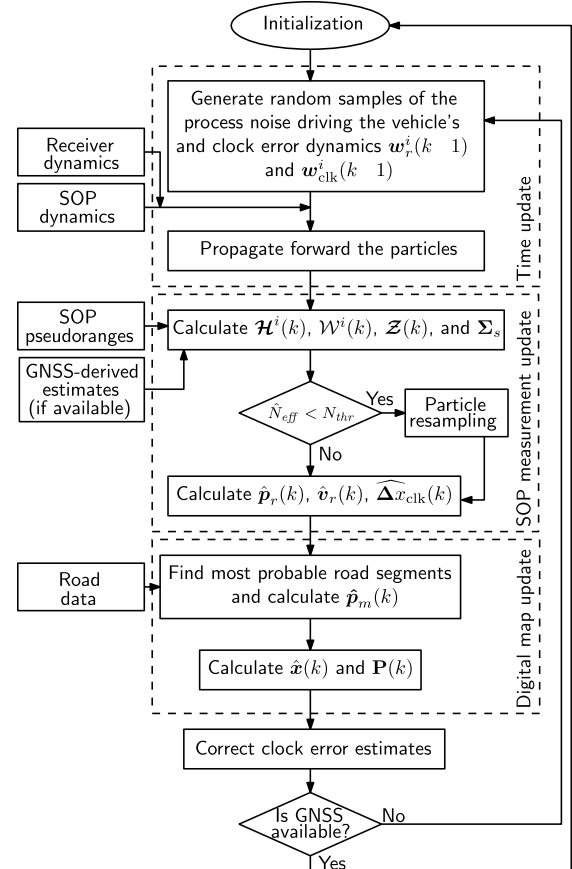


Fig. 3. Step-by-step summary of the proposed particle filter-based navigation solution. The proposed method consists of three parts: particle time update, SOP measurement update, and digital map update.

V. SIMULATION RESULTS

This section presents simulation results demonstrating the performance of the proposed method described in Section IV.

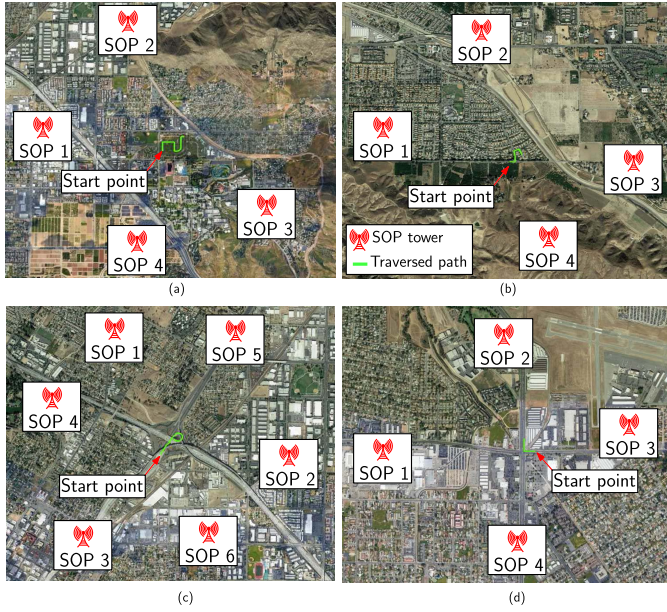


Fig. 4. The simulation environment layout, trajectory traversed by the vehicle, and position of SOP towers for different simulation tests: (a) Mode 1: straight segment then turn, (b) Mode 2, scenario 1: urban junctions, (c) Mode 2, scenario 2: highway, and (d) Mode 2, scenario 3: complete stop.

A simulated vehicle with initial access to GNSS (Mode 1) was assumed to navigate in an environment comprising multiple SOPs with a known location and unknown clock states. Pseudoranges from a varying number of SOP towers were simulated. The SOP towers were assumed to be equipped with oven-controlled crystal oscillators (OCXOs), while the vehicle-mounted receiver was assumed to be equipped with a temperature-compensated crystal oscillator (TCXO). The initial distances between the SOP towers and the vehicle were all assumed to be more than 1 km. The simulation settings are given in Table I. Note that in Table I, $\{\mathbf{p}_{r,j}(0)\}_{j=1}^4$ and $\{\mathbf{p}_{s_n,j}\}_{j=1}^4$ represent the vehicle's initial position (i.e., $\mathbf{p}_r(0)$) and the towers' positions (i.e., \mathbf{p}_{s_n}) corresponding to the j -th simulation test, respectively. The simulation environment layout and the trajectory traversed by the vehicle along with the position of the SOP towers for different simulation tests are illustrated in Fig. 4.

The particle filter was initialized with $\hat{\mathbf{x}}(k|k-1) \sim \mathcal{N}[\mathbf{x}(k), \mathbf{P}_x(k|k-1)]$, where $\mathbf{P}_x(k|k-1) \equiv \text{diag}[\mathbf{P}_p, \mathbf{P}_v, \mathbf{P}_{\Delta x_{\text{clk},s_n}}]$, $\mathbf{P}_p(k|k-1) \equiv (5) \cdot \text{diag}[1, 1]$, $\mathbf{P}_v(k|k-1) \equiv (5) \cdot \text{diag}[1, 1]$, $\mathbf{P}_{\Delta x_{\text{clk},s_n}}(k|k-1) \equiv \text{diag}[3, 0.3]$ for $n = 1, \dots, N_s$, and $\hat{\mathbf{x}}(k)$ is obtained according to the GNSS-derived estimates in Mode 1.

Navigation in Mode 1 and three different scenarios for navigation in Mode 2 were simulated spanning different driving conditions and access to GNSS signals:

- Mode 1: driving in a straight segment then turning. Here, the vehicle is assumed to have initial access to GNSS signals.
- Mode 2, scenario 1: driving in an urban environment with multiple junctions. Here, GNSS signals were unavailable.
- Mode 2, scenario 2: driving on a highway, while performing lane changing. Here, GNSS signals were unavailable.

TABLE I
SIMULATION SETTINGS

Parameter	Definition	Value
$\mathbf{p}_{r,1}(0)$	Vehicle initial position for Mode 1	[33.9804, -117.3305]
$\mathbf{p}_{r,2}(0)$	Vehicle initial position for Mode 2, scenario 1	[34.0374, -117.2239]
$\mathbf{p}_{r,3}(0)$	Vehicle initial position for Mode 2, scenario 2	[33.9917, -117.3581]
$\mathbf{p}_{r,4}(0)$	Vehicle initial position for Mode 2, scenario 3	[33.9458, -117.4530]
N	Number of particles	10 to 300 Particles
N_s	Number of SOP towers	3 to 6 towers
T	Sampling time	0.5 s
HDOP	Horizontal dilution of precision	1
G_p	Proportional term of the control loop	0.85
τ_{mp}	Gauss-Markov process time constant	1 s
σ^2_{mp}	Code phase multipath noise variance	1 m ² [65]
$\{\sigma^2_{s_n}\}_{n=1}^{N_s}$	Measurement noise variance	10 m ²
σ^2_m	Map displacement variance	2 m ²
$\Sigma_{\text{GNSS,nom}}$	GNSS-derived position error covariance	$5\mathbf{I}_{2 \times 2}$ m ² [65]
\tilde{q}_x	Acceleration noise power spectral densities	15 m ² /s ³
\tilde{q}_y	Acceleration noise power spectral densities	15 m ² /s ³
$\{S_{\tilde{w}_{\delta t,s_n}}\}_{n=1}^{N_s}$	Clock bias process noise power spectral density of transmitters	4×10^{-20} s
$\{S_{\tilde{w}_{\delta t,s_n}}\}_{n=1}^{N_s}$	Clock drift process noise power spectral density of transmitters	7.89×10^{-22} 1/s
$S_{\tilde{w}_{\delta t,r}}$	Clock bias process noise power spectral density of the receiver	4.7×10^{-20} s
$S_{\tilde{w}_{\delta t,r}}$	Clock drift process noise power spectral density of the receiver	7.5×10^{-20} 1/s
$\{\mathbf{p}_{s_n,1}\}_{n=1}^{N_s}$	Tower positions for Mode 1: straight segment then turning (with initial access to GNSS)	[33.9801, -117.3467; 33.9981, -117.3355; 33.9726, 117.3168; 33.9688, -117.3337]
$\{\mathbf{p}_{s_n,2}\}_{n=1}^{N_s}$	Tower positions for Mode 2, scenario 1: urban junction (without access to GNSS)	[34.0380, -117.2376; 34.0517, -117.2254; 34.0380, -117.2110; 34.0277, -117.2239]
$\{\mathbf{p}_{s_n,3}\}_{n=1}^{N_s}$	Tower positions for Mode 2, scenario 2: highway (without access to GNSS)	[33.9972, -117.3674; 34.0040, -117.3625; 33.9934, -117.3454; 33.9837, -117.3532; 33.9859, -117.3632]
$\{\mathbf{p}_{s_n,4}\}_{n=1}^{N_s}$	Tower positions for Mode 2, scenario 3: complete stop (without access to GNSS)	[33.9459, -117.4439; 33.9391, -117.4551; 33.9527, -117.4547; 33.9469, -117.4645]

- Mode 2, scenario 3: turning at a junction, while requires a complete stop before turning. Here, GNSS signals were unavailable.

TABLE II
MODE/SCENARIO DESCRIPTION

Mode/scenario	GNSS access	Number of towers	Path length (m)	Number of particles
Mode 1: Straight then turn	Yes	4	710	30
Mode 2, scenario 1: Urban junctions	No	4	280	10 to 100
Mode 2, scenario 2: Highway	No	3 to 6	440	30
Mode 2, scenario 3: Complete stop	No	4	270	30

Table II summarizes the main features of the different simulation tests.

Assuming the vehicle to stay centered in its driving lane, the road centerline was used as the ground truth. Based on this ground truth, the GNSS navigation solution and the pseudorange measurements drawn from SOPs were generated and corrupted with the additive noise tabulated in Table I. The following subsections present the achieved navigation results with the proposed framework.

A. Results for Mode 1: Straight Segment Then Turning (With Initial Access to GNSS)

The following scenario was simulated: a car that has access to GNSS, started driving in a straight segment heading up to a turning point. The true vehicle's position was corrupted by additive zero-mean Gaussian noise with a horizontal $\Sigma_{\text{GNSS, nom}}$ covariance. In order to simulate the multipath effect, a first-order Gauss-Markov process multipath model is used according to

$$\epsilon_{\text{mp}}(k+1) = e^{\frac{-T}{\tau_{\text{mp}}}} \epsilon_{\text{mp}}(k) + w_{\text{mp}}(k),$$

$$w_{\text{mp}} \sim \mathcal{N}\left[0, \frac{\sigma_{\text{mp}}^2 \tau_{\text{mp}}}{2} \left(1 - e^{\frac{-2T}{\tau_{\text{mp}}}}\right)\right],$$

where ϵ_{mp} is multipath model, T is the sampling time, τ_{mp} is Gauss-Markov process time constant, w_{mp} is the driving noise, and σ_{mp} is the GNSS code phase multipath noise standard deviation. Note that for a dual-frequency (f_1, f_2) GNSS receiver, σ_{mp} is replaced with

$$\sigma_{\text{mp}} \leftarrow \sigma_{\text{mp}} \sqrt{\left[\frac{f_1^2}{f_1^2 - f_2^2}\right]^2 + \left[\frac{f_2^2}{f_1^2 - f_2^2}\right]^2}.$$

The use of a first-order Gauss-Markov process to model the multipath has been proposed and validated by prior work [60], [62]. During the period of this simulation, the vehicle-mounted receiver produced pseudoranges to four SOPs. Fig. 5 illustrates the traversed path by the vehicle before GNSS become unavailable. It can be seen from Fig. 5 that the estimated position follows closely the ground truth. Moreover, the simulation results demonstrated that the proposed framework achieved a position RMSE of 2.62 m over a trajectory of 800 m while the GNSS-only navigation solution achieved a position RMSE of 4.43 m over a same trajectory. Hence,

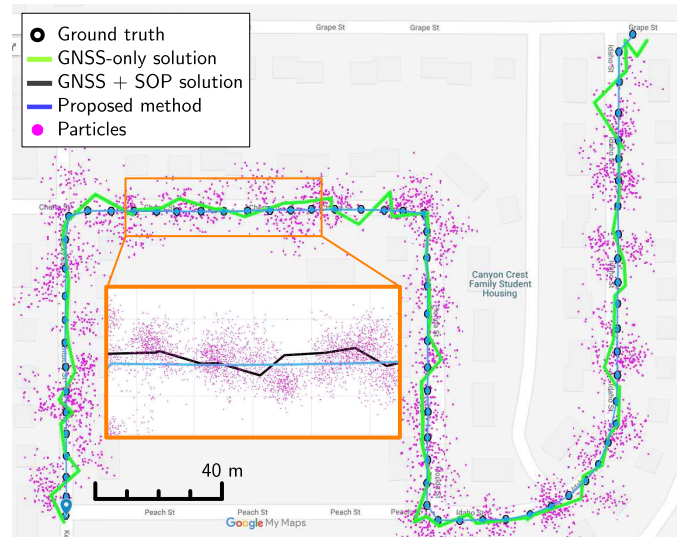


Fig. 5. Simulation results for Mode 1: straight segment then turning (with initial access to GNSS). Note that the green line was obtained by only using GNSS pseudoranges to emulate a low-cost technology.

TABLE III
NAVIGATION PERFORMANCE COMPARISON DUE TO DIFFERENT PARTICLE NUMBERS

Particle Numbers	RMSE	Standard deviation	Max. Error
10	5.6 m	2.5 m	12.5 m
30	2.2 m	1.4 m	10.5 m
50	1.9 m	1.1 m	3.4 m
100	1.9 m	0.9 m	3.1 m

incorporating the proposed framework reduced the position RMSE by 40.86% in Mode 1.

B. Results for Mode 2, Scenario 1: Urban Junction (Without Access to GNSS)

This scenario considered a vehicle driving in an urban street with multiple junctions. The vehicle did not have access to GNSS signals. The test data was simulated on a street in Riverside, California, USA. The data was sampled at 2 Hz. The vehicle drove for 280 m including one crossroads and two three ways. For this simulation, the number of particles was chosen to be 30. Fig. 6 illustrates the achieved results. The white circles represent digital map points (not necessarily the traversed path) and the circles filled with blue represent the ground truth (the traversed path). It can be seen that the particles follow the ground truth closely and the behavior of the discrepancy of particles is consistent even across the junctions. The RMSE of the vehicle's position with the SOP-only navigation solution was found to be 4.24 m, whereas the RMSE using the proposed map-matching technique was 2.2 m. For a comparative analysis, this simulation was performed using different particle numbers: $N = 10, 30, 50, 100$. Table III compares the navigation performance due to different particle numbers.

The following may be concluded from this simulation. First, the proposed map-matching method reduced the RMSE by 48.11% from the SOP-only navigation solution. Second,

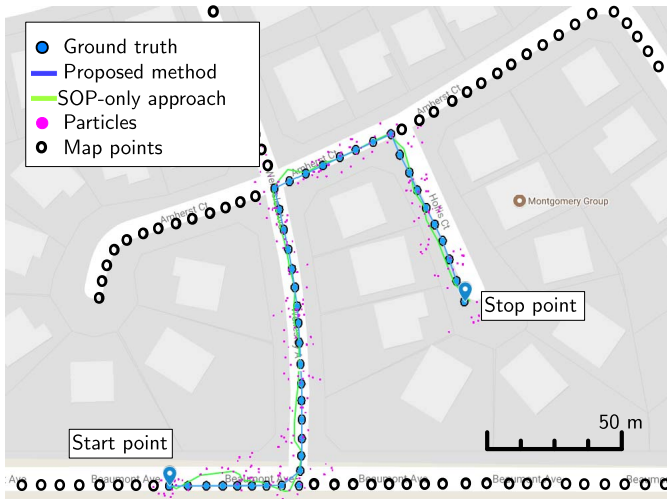


Fig. 6. Simulation results for Mode 2, scenario 1: urban junction (without access to GNSS). Only one-tenth of the particles were plotted to make the navigation solutions visible.

TABLE IV
POSITION ESTIMATION ERROR FOR DIFFERENT MAP-MATCHING SCENARIOS IN MODE 2

Mode 2 Scenario:	SOP-only RMSE	Proposed approach RMSE	Improvement
1: Urban junctions	4.24 m	2.2 m	48.11 %
2: Highway	2.42 m	0.97 m	59.91 %
3: Complete stop	4.93 m	1.28 m	74.03 %

using 30 particles for driving in an urban street with multiple junctions would be sufficient for precise navigation while using fewer particles may result in particle discrepancy in junctions and an increase in the RMSE.

C. Results for Mode 2, Scenario 2: Highway (Without Access to GNSS)

This scenario considered a vehicle driving on the highway at 100 km/h. The GNSS signals were not available in this scenario. The test data was simulated on a street in Riverside, California, USA, which is shown in Fig. 7. It can be seen that the vehicle started moving in the north-east direction. After 200 m, it changed its lane (one lane to the right), and after another 200 m it made a right turn heading north-west. The number of particles was chosen to be $N = 50$, and it was found with several runs that increasing the number of particles to $N > 50$ yielded negligible performance improvement. Fig. 7 illustrates the achieved results. It can be seen that the map-matched estimates followed the ground truth closely. The navigation error is tabulated in Table IV.

In order to evaluate the impact of the number of SOPs N_s on the navigation solution, this test was conducted for $N_s = 3, 4, 5, 6$ SOPs. The results are tabulated in Table V. The following can be concluded from this simulation. First, with $N_s = 4$, the proposed map-matching approach achieved an RMSE of 0.97 m compared to an RMSE of 2.42 m with an SOP-only navigation solution (See Table IV). The achieved

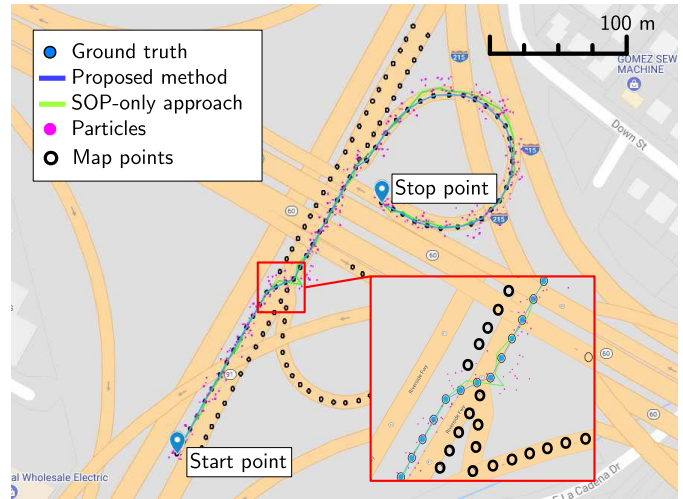


Fig. 7. Simulation results for Mode 2, scenario 2: highway (without access to GNSS). Only one-tenth of the particles were plotted and map points only around the traversed path are displayed to make the navigation solutions visible.

TABLE V
IMPACT OF THE NUMBER OF SOPs ON THE NAVIGATION SOLUTION

Number of SOPs	SOP-Only		Proposed approach	
	RMSE	Max. Error	RMSE	Max. Error
3	5.93 m	15.16 m	1.35 m	8.58 m
4	2.42 m	6.37 m	0.97 m	4.42 m
5	1.82 m	7.02 m	0.91 m	3.51 m
6	1.76 m	4.13 m	0.88 m	2.97 m

precision is important for lane-changing driving. Second, as can be seen from Table V, the proposed map-matching approach achieved significantly lower estimation error with fewer towers than the case with SOP-Only navigation solution.

D. Results for Mode 2, Scenario 3: Complete Stop (Without Access to GNSS)

This scenario considered a vehicle driving at a crossroad. GNSS signals were unavailable in this scenario. The vehicle started by moving in the north direction. After 100 m it entered a crossroad and performed a complete stop. After five seconds, it made a right turn to head east. As stated in Subsection III-A, receiver and SOP clock biases are dynamic and stochastic. Therefore, if the vehicle is stationary (e.g., when coming to a complete stop at a turning junction) the clocks are drifting and the navigation solution will naturally drift as time-varying clock biases cannot be distinguished from change in the true range due to the vehicle's motion. This scenario evaluates the performance of the proposed approach under this driving condition.

Fig. 8 illustrates the map-matching results for this scenario. The RMSE using SOP-only navigation solution was found to be 4.93 m, while the proposed method reduced this error to 1.28 m (See Table IV).

It is worth noting that the vehicle's dynamical model was assumed to evolve according to a velocity random walk model

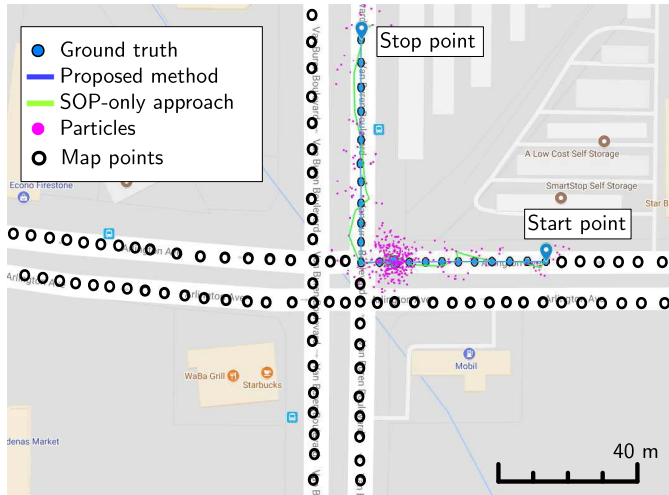


Fig. 8. Simulation results for Mode 2, scenario 3: complete stop (without access to GNSS). Only one-tenth of the particles were plotted to make the navigation solutions visible.

(cf. (3)), which does not hold for the vehicle coming at a complete stop (unless the process noise is set to zero). Despite this model mismatch, the performance of the proposed approach achieved a RMSE of 1.28 m, which is a 74 % improvement over the SOP-only navigation solution. In order to improve the performance even further, an interacting multiple model (MM)-type filter can be employed for the transition between stationary and mobile vehicle. In practice, the vehicle would be equipped with an inertial measurement unit (IMU) to propagate the vehicle's position and velocity states between SOP measurements.

VI. EXPERIMENTAL RESULTS

To evaluate the performance of the proposed algorithm, three experiments were performed using ambient cellular LTE SOPs and a ground vehicle navigation in (i) an urban environment where multipath severely affects the received LTE signals, (ii) a suburban environment where LTE SOPs have poor geometric diversity, and (iii) a challenging urban environment with multiple junctions and GNSS cutoff conditions, while using pseudorange measurements from only 2 LTE SOPs. This section shows that the proposed algorithm improves the navigation solution in all these environments. The following subsections present the experimental setup and the results for each environment.

A. Experimental Setup and Scenario Description

A ground vehicle was equipped with two consumer-grade 800/1900 MHz cellular omnidirectional Laird antennas to receive LTE signals at two different carrier frequencies. The signals were simultaneously down-mixed and synchronously sampled via a National Instruments (NI) dual-channel universal software radio peripheral (USR)-2954R[®], driven by a GPS-disciplined oscillator (GSPDO). The clock bias and drift process noise power spectral densities of the receiver were set to be 1.3×10^{-22} s and 7.89×10^{-25} 1/s respectively, according to the oven-controlled crystal oscillator (OCXO) used in a USRP-2954R[®]. The measurement noise variances



Fig. 9. Experimental hardware and software setup.

TABLE VI
SCENARIO DESCRIPTION OF EXPERIMENTS

Environment	Number of LTE SOPs	Path length	Number of particles
Urban	5	825 m	30
Suburban	2	1500 m	30
Challenging	2	345 m	30

$\{\sigma_{s_n}^2\}_{n=1}^{N_s}$ were set to be 10 m^2 . The LTE and GNSS signals were stored on a laptop for off-line post-processing. The LTE signals were processed and pseudoranges were obtained using the Multichannel Adaptive TRAnsciever Information eXtractor (MATRIX) SDR [34]. The proposed algorithm was used to obtain the LTE navigation solution and the results were compared with the ground truth. To obtain a reliable and accurate ground truth, the vehicle was also equipped with a Septentrio AsteRx-i V integrated GNSS-IMU [66], which includes a dual-antenna, multi-frequency GNSS receiver, and a Vectornav VN-100 micro-electromechanical system (MEMS) IMU. Septentrio's post-processing software development kit (PP-SDK) was used to process the carrier phase observables collected by the AsteRx-i V and by a nearby differential GPS base station to obtain a carrier phase-based navigation solution. Finally, the integrated GNSS-IMU real-time kinematic (RTK) system was used to produce the ground truth results with which the proposed navigation solution was compared. Fig. 9 shows the experimental setup and Table VI summarizes the scenario description for the three experiments.

B. Experimental Results for Urban Environment

The first experiment was conducted in an urban environment (downtown Riverside, California, USA). It is worth mentioning that due to the lower elevation angles of LTE towers compared to the GNSS satellites, the effect of multipath on LTE signals is typically significantly higher than GNSS signals in urban environments.

In this experiment, the integrated GNSS-IMU system was used to provide the ground truth along the entire trajectory. However, the navigation solution obtained from the

TABLE VII
CHARACTERISTICS OF LTE TOWERS USED IN URBAN ENVIRONMENT EXPERIMENT

LTE SOP	Carrier frequency (MHz)	Cell ID	Bandwidth (MHz)
1	1955	216	20
2	739	319	10
3	739	288	10
4	739	151	10
5	739	232	10

TABLE VIII
NAVIGATION PERFORMANCE COMPARISON IN AN URBAN ENVIRONMENT

Performance measure	LTE-only navigation solution	Proposed approach	Improvement
RMSE	6.37 m	1.6 m	74.88%
Standard deviation	2.09 m	0.65 m	68.9%
Max. error	11.18 m	3.74 m	66.55%

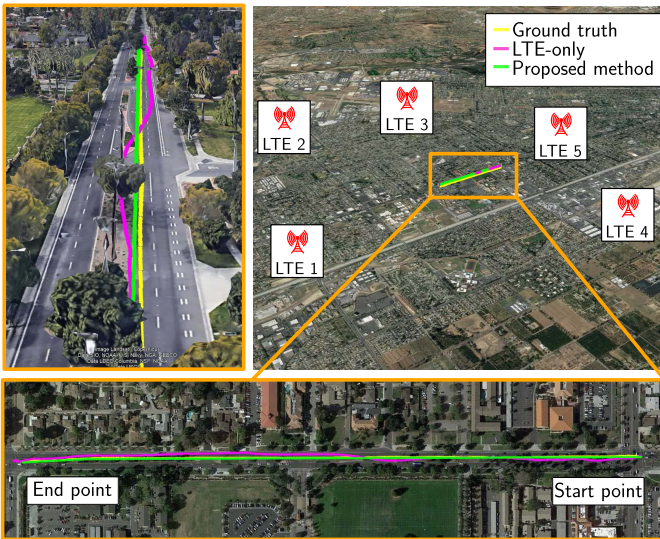


Fig. 10. The environment layout, LTE SOP positions, true vehicle trajectory, LTE-only navigation solution using the method presented in [67], and estimated vehicle trajectory using the proposed algorithm. Image: Google Earth.

GNSS-IMU system is discarded to emulate a GNSS cutoff period. Over the course of the experiment, the ground vehicle traversed 825 m while listening to 5 LTE SOP towers. All LTE towers belonged to the U.S. cellular provider AT&T with the characterisation summarized in Table VII.

Fig. 10 shows the environment layout, LTE SOP positions, true vehicle trajectory, LTE-only navigation solution, and estimated vehicle trajectory using the proposed closed-loop map-matching algorithm. Table VIII compares the navigation performance obtained by the proposed algorithm versus that of the LTE-only navigation solution. It can be seen that incorporating the proposed map-matching algorithm reduced the position RMSE by 74.88% from the RMSE obtained by a LTE-only navigation solution.

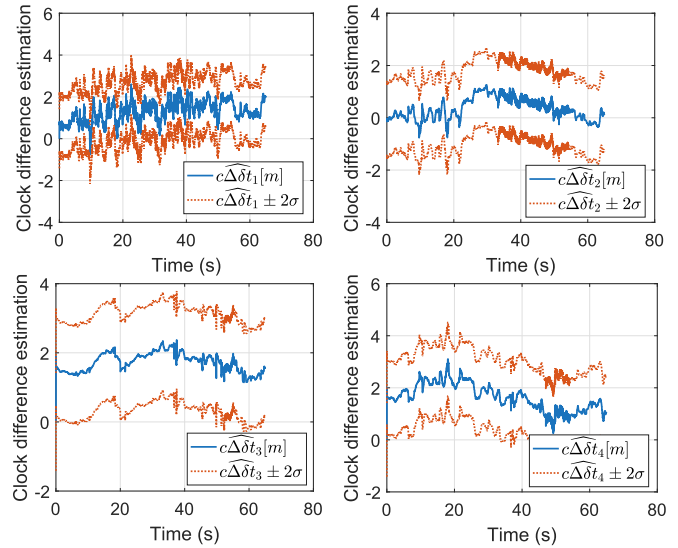


Fig. 11. Estimated difference between the receiver's clock bias and each LTE SOP clock bias and corresponding variance.

TABLE IX
ESTIMATION PERFORMANCE WITH AND WITHOUT CLOCK DIFFERENCE CORRECTION

Method	RMSE	% Of incorrectly map-matched points
Open-loop	3.69 m	7.5%
Closed-loop	1.6 m	1.9%

Fig. 11 shows the estimated difference between the receiver's and each LTE SOP's clock biases and corresponding variances. It can be seen that using the proposed algorithm the estimated variances remain stable in the course of the experiment. Since the actual receiver's and eNodeBs' clock biases are not available, it is impossible to show the estimation errors.

Next, the effect of the clock difference correction (cf. (12)) on the achievable accuracy was evaluated. To this end, the stored data of this experiment was processed with and without clock difference correction. The results are shown in Table IX. In this table, the RMSE of the estimated position as well as the percentage of the points, which were incorrectly map-matched, are tabulated. As can be seen, the proposed closed-loop framework (i.e., with clock difference correction) significantly improves the open-loop solution accuracy (i.e., without clock difference correction).

C. Experimental Results for Suburban Environment

The second experiment was conducted in a suburban environment, using only 2 LTE SOP towers with poor geometry. Over the course of the experiment, the vehicle-mounted receiver traversed a total trajectory of 1.5 km while listening to 2 LTE SOPs simultaneously. Characteristics of the LTE SOPs are presented in Table X.

This experiment studied the performance as the vehicle turned along the road, crossed junctions, and came to a complete stop. Fig. 12 shows the environment layout, LTE

TABLE X

CHARACTERISTICS OF LTE TOWERS USED IN SUBURBAN ENVIRONMENT

LTE SOP	Operator	Carrier frequency (MHz)	Cell ID	Bandwidth (MHz)
1	T-Mobile	2145	21	20
2	AT&T	1955	300	20

TABLE XI

NAVIGATION PERFORMANCE COMPARISON IN A SUBURBAN ENVIRONMENT

Performance measure	LTE-only navigation solution	Proposed approach	Improvement
RMSE	9.32 m	3.9 m	58.15%
Standard deviation	4.36 m	2.76 m	36.69%
Max. error	33.47 m	14.91 m	55.45%

TABLE XII

CHARACTERISTICS OF LTE TOWERS USED IN THE THIRD EXPERIMENT

LTE SOP	Operator	Carrier frequency (MHz)	Cell ID	Bandwidth (MHz)
1	T-Mobile	2145	79	20
2	AT&T	1955	350	20

SOP positions, true vehicle trajectory, LTE-only navigation solution provided in [68], and estimated vehicle trajectory using the proposed algorithm. Table XI compares the navigation performance obtained by the proposed algorithm versus that of the LTE-only navigation solution. It can be seen that the proposed approach is robust in areas with poor geometric diversity and a limited number of LTE SOPs. The experimental results show that the incorporating the proposed map-matching algorithm reduced the position RMSE by 58.15% from the RMSE obtained by a LTE-only navigation solution.

D. Experimental Results for a Challenging Urban Environment

To assess the robustness of the proposed framework, the third experiment was conducted in a challenging environment in downtown Riverside, California. Here, an urban street with multiple junctions was chosen. The duration of the drive test was 70 s, including 9 s of complete stop before the cross junction in a GNSS cutoff condition. The streets were surrounded by tall buildings from both sides and only 2 LTE towers were available in the environment. Over the course of the experiment, the vehicle traveled 345 m while listening to only 2 LTE towers with characteristics summarized in Table XII.

The ground truth was produced using GNSS-IMU RTK system described in Subsection VI-A. The GPS-only navigation solution was obtained by only using GPS pseudoranges to emulate a low-cost technology. To evaluate the performance of the proposed framework in the absence of GPS signals, while using signals from only 2 LTE transmitters, the GPS-only

TABLE XIII

NAVIGATION PERFORMANCE COMPARISON IN A GNSS-CHALLENGED URBAN ENVIRONMENT

Performance measure	GPS-only navigation solution	GPS-LTE navigation solution	Proposed approach	Improvement over GPS-LTE
RMSE	11.26 m	6.69 m	3.6 m	46.18%
Standard deviation	7.68 m	3.87 m	3.02 m	21.96%
Max. error	18.15 m	15.55 m	11.7 m	27.75%

navigation solution was discarded over a portion of 90 m of the total trajectory.

Fig. 13 demonstrates the environment layout along with the location of the LTE transmitters, true vehicle trajectory, GPS-only navigation solution, GPS-LTE navigation solution, and the estimated vehicle trajectory using the proposed framework. GPS cutoff point, GPS back in point, and the vehicle's stop point at the cross junction is also demonstrated in this figure. Moreover, the effect of the clock difference correction (cf. (12)) on the achievable accuracy is shown. Table XIII compares the navigation performance of the proposed framework versus that of the GPS-only and GPS-LTE navigation solutions. The following may be concluded from these results. First, when GPS signals were unavailable the GPS-only navigation solution drifted from the ground truth. This is due to the fact that the aiding corrections from GPS signals were not available. As expected, the proposed framework did not exhibit this drift as LTE signals were used as an aiding source. Second, it can be seen from these results that the proposed closed-loop map-matching navigation framework outperforms the GPS-LTE solutions. The results demonstrated a position RMSE of 6.69 m using GPS-LTE framework and RMSE of 3.6 m using the proposed close-loop map-matching method. Hence, incorporating the presented method reduced the position RMSE by 46.18 %.

VII. CONCLUSION AND FUTURE WORK

A method for ground vehicle localization in GNSS-challenged environments using road information from digital maps and ambient LTE SOPs was proposed. The main contribution of the work was to develop a closed-loop particle filter-based framework that fuses LTE pseudoranges with digital maps to estimate the vehicle's state, simultaneously with the difference between the vehicle-mounted receiver's and LTE SOPs' clock bias and drift. The proposed method used a displacement information as a feedback source to continuously estimate the clock states for all LTE transmitters. The proposed approach operates in two modes: GNSS signals are available (Mode 1) and GNSS signals are unavailable (Mode 2). Simulation and experimental results were presented demonstrating the efficacy and accuracy of the proposed framework in different driving environments (urban and suburban) and under different driving conditions (junctions, highway with lane change,

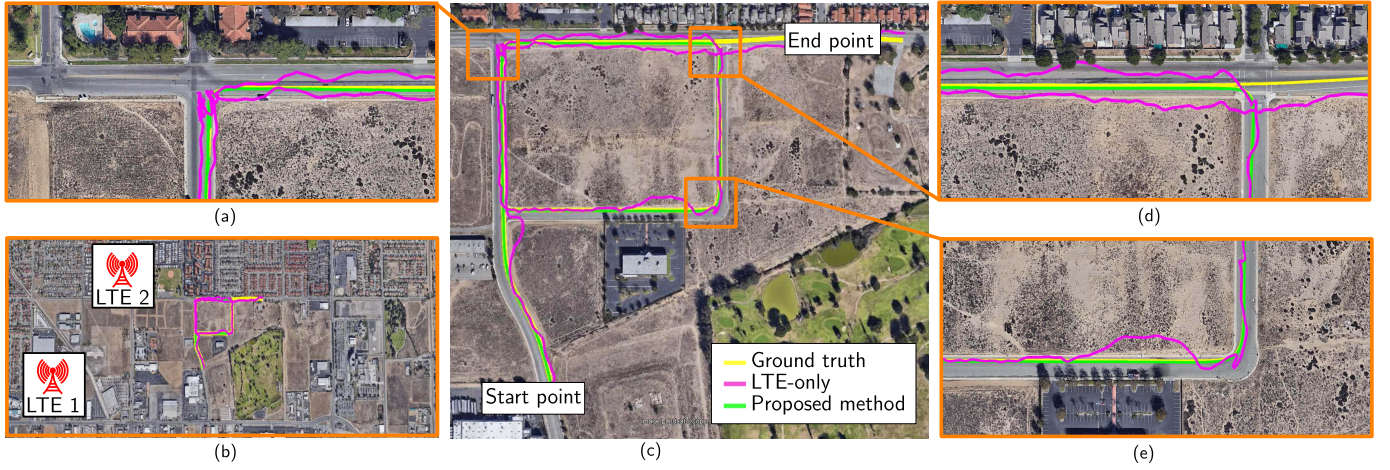


Fig. 12. Environment layout, LTE SOPs' positions, true vehicle trajectory, LTE-only navigation solution, and estimated vehicle trajectory using the proposed algorithm. (a) Complete stop before turning point, (b) LTE SOPs' positions, (c) vehicle's trajectory and environment layout, (d) junction point, and (e) turning point. Image: Google Earth.



Fig. 13. The environment layout along with the location of LTE transmitters, true vehicle trajectory, GPS-only navigation solution, GPS-LTE navigation solution, and estimated vehicle trajectory using the proposed algorithm. Image: Google Earth.

and complete stop). The experimental results demonstrated a position RMSE of (i) 1.6 m over a 825 m trajectory in an urban environment with 5 LTE SOPs, (ii) 3.9 m over a 1.5 km trajectory in a suburban environment with 2 LTE SOPs, and (iii) 3.6 m over a 345 m trajectory in a challenging urban environment with 2 LTE SOPs. Moreover, it was demonstrated that incorporating the proposed map-matching algorithm reduced the position RMSE by 74.88% and 58.15% in urban and suburban environments, respectively, from the RMSE obtained by a LTE-only navigation.

While this paper considered a simple feedback mechanism, more sophisticated feedback algorithms, such as multi-

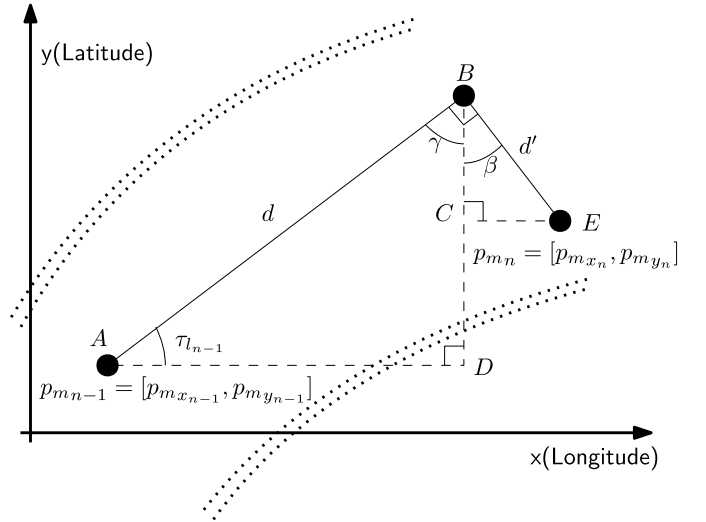


Fig. 14. Calculating the latitude and longitude of the n -th map-matched point in a sample link l .

hypothesis, could be investigated in future work in an attempt to improve the robustness. In addition, while this work considered a simple statistical model for the vehicle dynamics, future work could consider using other sensors (e.g., lidar and INS) to obtain the vehicle's odometry, which reduces the model mismatch between the assumed vehicle's dynamics model and the vehicle's true motion. Moreover, the problem of storing and maintaining a database that includes the location of SOP transmitters could be investigated in future work.

APPENDIX A DERIVATION OF EQUATION (4)

Fig. 14 illustrates $(n - 1)$ -th and n -th map-matched points in link l . The distance between two adjacent points in a road centerline takes the form

$$d = s_{l_n} - s_{l_{n-1}}.$$

Thus,

$$\begin{aligned}\overline{AD} &= (s_{l_n} - s_{l_{n-1}}) \cos(\tau_{l_{n-1}}), \\ \overline{BD} &= (s_{l_n} - s_{l_{n-1}}) \sin(\tau_{l_{n-1}}).\end{aligned}$$

The distance $d' = \alpha k_{l_n}$ where α and k_{l_n} represent lane width and lane identifier, respectively, for the n -th map-matched point. As can be seen from Fig. 14

$$\begin{aligned}\beta + \gamma &= 90^\circ, \\ \tau_{l_{n-1}} + \gamma &= 90^\circ.\end{aligned}$$

Thus, the angle β equals the heading angle of the previous point $\tau_{l_{n-1}}$. Therefore,

$$\begin{aligned}\overline{CE} &= \alpha k_{l_n} \sin(\tau_{l_{n-1}}), \\ \overline{BC} &= \alpha k_{l_n} \cos(\tau_{l_{n-1}}).\end{aligned}$$

The coordinates of n -th map-matched point can be computed based on the $(n-1)$ -th point according to

$$\begin{aligned}p_{m_{x_n}} &= p_{m_{x_{n-1}}} + \overline{AD} + \overline{CE}, \\ p_{m_{y_n}} &= p_{m_{y_{n-1}}} + \overline{BD} - \overline{BC},\end{aligned}$$

which yields

$$\begin{aligned}\mathcal{M}_l &= p_{m_{x_{n-1}}} + (s_{l_n} - s_{l_{n-1}}) \cos(\tau_{l_{n-1}}) + \alpha k_{l_n} \sin(\tau_{l_{n-1}}), \\ \mathcal{N}_l &= p_{m_{y_{n-1}}} + (s_{l_n} - s_{l_{n-1}}) \sin(\tau_{l_{n-1}}) - \alpha k_{l_n} \cos(\tau_{l_{n-1}}).\end{aligned}$$

ACKNOWLEDGMENT

The authors would like to thank Kimia Shamaei for her help with the data collection.

REFERENCES

- [1] N. Greenblatt, "Self-driving cars and the law," *IEEE Spectrum*, vol. 53, no. 2, pp. 46–51, Feb. 2016.
- [2] J. Du and M. Barth, "Next-generation automated vehicle location systems: Positioning at the lane level," *IEEE Trans. Intell. Transp. Syst.*, vol. 9, no. 1, pp. 48–57, Mar. 2008.
- [3] T. Luettel, M. Himmelsbach, and H. Wuensche, "Autonomous ground vehicles—Concepts and a path to the future," *Proc. IEEE*, vol. 100, no. Special Centennial Issue, pp. 1831–1839, May 2012.
- [4] I. Skog and P. Handel, "In-car positioning and navigation technologies—A survey," *IEEE Trans. Intell. Transp. Syst.*, vol. 10, no. 1, pp. 4–21, Mar. 2009.
- [5] R. Toledo-Moreo, M. Zamora-Izquierdo, B. Ubeda-Miarro, and A. Gomez-Skarmeta, "High-integrity IMM-EKF-based road vehicle navigation with low-cost GPS/SBAS/INS," *IEEE Trans. Intell. Transp. Syst.*, vol. 8, no. 3, pp. 491–511, Sep. 2007.
- [6] A. Soloviev, "Tight coupling of GPS, INS, and laser for urban navigation," *IEEE Trans. Aerosp. Electron. Syst.*, vol. 46, no. 4, pp. 1731–1746, Oct. 2010.
- [7] H. Liu, S. Nassar, and N. El-Sheimy, "Two-filter smoothing for accurate INS/GPS land-vehicle navigation in urban centers," *IEEE Trans. Veh. Technol.*, vol. 59, no. 9, pp. 4256–4267, Nov. 2010.
- [8] A. Vu, A. Ramanandan, A. Chen, J. Farrell, and M. Barth, "Real-time computer vision/DGPS-aided inertial navigation system for lane-level vehicle navigation," *IEEE Trans. Intell. Transp. Syst.*, vol. 13, no. 2, pp. 899–913, Jun. 2012.
- [9] R. Toledo-Moreo, D. Betaille, and F. Peyret, "Lane-level integrity provision for navigation and map matching with GNSS, dead reckoning, and enhanced maps," *IEEE Trans. Intell. Transp. Syst.*, vol. 11, no. 1, pp. 100–112, Mar. 2010.
- [10] M. Atia *et al.*, "A low-cost lane-determination system using GNSS/IMU fusion and HMM-based multistage map matching," *IEEE Trans. Intell. Transp. Syst.*, vol. 18, no. 11, pp. 3027–3037, Nov. 2017.
- [11] G. Jagadeesh and T. Srikanthan, "Online map-matching of noisy and sparse location data with hidden Markov and route choice models," *IEEE Trans. Intell. Transp. Syst.*, vol. 18, no. 9, pp. 2423–2434, Sep. 2017.
- [12] Z. Peng, S. Gao, B. Xiao, S. Guo, and Y. Yang, "CrowdGIS: Updating digital maps via mobile crowdsensing," *IEEE Trans. Autom. Sci. Eng.*, to be published.
- [13] E. Costa, "Simulation of the effects of different urban environments on GPS performance using digital elevation models and building databases," *IEEE Trans. Intell. Transp. Syst.*, vol. 12, no. 3, pp. 819–829, Sep. 2011.
- [14] J. Grabowski, "Personal privacy jammers: Locating jersey PPDs jamming GBAS safety-of-life signals," in *GPS World Magazine*, Apr. 2012, pp. 28–37.
- [15] C. Günther, "A survey of spoofing and counter-measures," *NAVIGATION J. Inst. Navigat.*, vol. 61, no. 3, pp. 159–177, 2014.
- [16] L. Merry, R. Faragher, and S. Schedin, "Comparison of opportunistic signals for localisation," in *Proc. IFAC Symp. Intell. Auton. Veh.*, Sep. 2010, pp. 109–114.
- [17] K. Pesyna, Z. Kassas, J. Bhatti, and T. Humphreys, "Tightly-coupled opportunistic navigation for deep urban and indoor positioning," in *Proc. ION GNSS Conf.*, Sep. 2011, pp. 3605–3617.
- [18] Z. Kassas, "Collaborative opportunistic navigation," *IEEE Aerosp. Electron. Syst. Mag.*, vol. 28, no. 6, pp. 38–41, 2013.
- [19] Z. Kassas, "Analysis and synthesis of collaborative opportunistic navigation systems," Ph.D. dissertation, Dept. Elect. Comput. Eng., Univ. Texas Austin, Austin, TX, USA, 2014.
- [20] G. De Angelis, G. Baruffa, and S. Cacopardi, "GNSS/Cellular hybrid positioning system for mobile users in urban scenarios," *IEEE Trans. Intell. Transp. Syst.*, vol. 14, no. 1, pp. 313–321, Mar. 2013.
- [21] M. Driusso, C. Marshall, M. Sabathy, F. Knutti, H. Mathis, and F. Babich, "Vehicular position tracking using LTE signals," *IEEE Trans. Veh. Technol.*, vol. 66, no. 4, pp. 3376–3391, Apr. 2017.
- [22] K. Shamaei, J. Khalife, and Z. Kassas, "Exploiting LTE signals for navigation: Theory to implementation," *IEEE Trans. Wireless Commun.*, vol. 17, no. 4, pp. 2173–2189, Apr. 2018.
- [23] J. Khalife and Z. Kassas, "Navigation with cellular CDMA signals—Part II: Performance analysis and experimental results," *IEEE Trans. Signal Process.*, vol. 66, no. 8, pp. 2204–2218, Apr. 2018.
- [24] P. Thevenon *et al.*, "Positioning using mobile TV based on the DVB-SH standard," *NAVIGATION, J. Inst. Navigat.*, vol. 58, no. 2, pp. 71–90, 2011.
- [25] C. Yang, T. Nguyen, and E. Blasch, "Mobile positioning via fusion of mixed signals of opportunity," *IEEE Aerosp. Electron. Syst. Mag.*, vol. 29, no. 4, pp. 34–46, Apr. 2014.
- [26] J. McElroy, "Navigation using signals of opportunity in the AM transmission band," M.S. thesis, Air Force Inst. Technol., Wright-Patterson Air Force Base, Ohio, USA, 2006.
- [27] S. Fang, J. Chen, H. Huang, and T. Lin, "Is FM a RF-based positioning solution in a metropolitan-scale environment? A probabilistic approach with radio measurements analysis," *IEEE Trans. Broadcast.*, vol. 55, no. 3, pp. 577–588, Sep. 2009.
- [28] J. Morales, J. Khalife, C. Ardito, and Z. Kassas, "Simultaneous tracking of orbcomm LEO satellites and inertial navigation system aiding using Doppler measurements," in *Proc. IEEE Veh. Technol. Conf.*, 2019.
- [29] C. Ardito, J. Morales, J. Khalife, A. Abdallah, and Z. Kassas, "Performance evaluation of navigation using LEO satellite signals with periodically transmitted satellite positions," in *Proc. ION Int. Tech. Meeting Conf.*, 2019.
- [30] J. Morales, P. Roysdon, and Z. Kassas, "Signals of opportunity aided inertial navigation," in *Proc. ION GNSS Conf.*, Sep. 2016, pp. 1492–1501.
- [31] Z. Kassas, J. Morales, K. Shamaei, and J. Khalife, "LTE steers UAV," *GPS World Mag.*, vol. 28, no. 4, pp. 18–25, Apr. 2017.
- [32] J. Khalife, S. Ragothaman, and Z. Kassas, "Pose estimation with lidar odometry and cellular pseudorange," in *Proc. IEEE Intell. Veh. Symp.*, Jun. 2017, pp. 1722–1727.
- [33] M. Maaref, J. Khalife, and Z. Kassas, "Lane-level localization and mapping in GNSS-challenged environments by fusing lidar data and cellular pseudorange," *IEEE Trans. Intell. Veh.*, vol. 4, no. 1, pp. 73–89, Mar. 2019.
- [34] Z. Kassas, J. Khalife, K. Shamaei, and J. Morales, "I hear, therefore I know where I am: Compensating for GNSS limitations with cellular signals," *IEEE Signal Process. Mag.*, pp. 111–124, Sep. 2017.

- [35] J. del Peral-Rosado *et al.*, "Software-defined radio LTE positioning receiver towards future hybrid localization systems," in *Proc. Int. Commun. Satellite Syst. Conf.*, Oct. 2013, pp. 14–17.
- [36] J. Khalife, K. Shamaei, and Z. Kassas, "Navigation with cellular CDMA signals—Part I: Signal modeling and software-defined receiver design," *IEEE Trans. Signal Process.*, vol. 66, no. 8, pp. 2191–2203, Apr. 2018.
- [37] Y. Zhao, Q. Qin, J. Li, C. Xie, and R. Chen, "Highway map matching algorithm based on floating car data," in *Proc. IEEE Int. Geosci. Remote Sens. Symp.*, Jul. 2012, pp. 5982–5985.
- [38] Z. He, S. Xi-Wei, L. Zhuang, and P. Nie, "Online map-matching framework for floating car data with low sampling rate in urban road networks," *IET Intell. Transp. Syst.*, vol. 7, no. 4, pp. 404–414, Dec. 2013.
- [39] M. Rohani, D. Gingras, and D. Gruyer, "A novel approach for improved vehicular positioning using cooperative map matching and dynamic base station DGPS concept," *IEEE Trans. Intell. Transp. Syst.*, vol. 17, no. 1, pp. 230–239, Jan. 2016.
- [40] R. Mohamed, H. Aly, and M. Youssef, "Accurate real-time map matching for challenging environments," *IEEE Trans. Intell. Transp. Syst.*, vol. 18, no. 4, pp. 847–857, Apr. 2017.
- [41] K. ElMokhtari, S. Reboul, J. Choquel, G. Stienne, B. Amami, and M. Benjelloun, "Circular particle fusion filter applied to map matching," *IET Intell. Transport Syst.*, vol. 11, no. 8, pp. 491–500, Oct. 2017.
- [42] K. Zhang, S. Liu, Y. Dong, D. Wang, Y. Zhang, and L. Miao, "Vehicle positioning system with multi-hypothesis map matching and robust feedback," *IET Intell. Transp. Syst.*, vol. 11, no. 10, pp. 649–658, Nov. 2017.
- [43] M. Hashemi, "Reusability of the output of map-matching algorithms across space and time through machine learning," *IEEE Trans. Intell. Transp. Syst.*, vol. 18, no. 11, pp. 3017–3026, Nov. 2017.
- [44] M. Najjar and P. Bonnifait, "A road-matching method for precise vehicle localization using belief theory and kalman filtering," *Auton. Robots*, vol. 19, no. 2, pp. 173–191, Sep. 2005.
- [45] M. Yu, Z. Li, Y. Chen, and W. Chen, "Improving integrity and reliability of map matching techniques," *J. Global Positioning Syst.*, vol. 1, no. 10, pp. 40–46, Dec. 2006.
- [46] M. Quddus, W. Ochieng, and R. Noland, "Current map-matching algorithms for transport applications: State-of-the art and future research directions," *Transp. Res. C, Emerg. Technol.*, vol. 15, no. 5, pp. 312–328, May 2007.
- [47] Z. Kassas and T. Humphreys, "Observability analysis of collaborative opportunistic navigation with pseudorange measurements," *IEEE Trans. Intell. Transp. Syst.*, vol. 15, no. 1, pp. 260–273, Feb. 2014.
- [48] Z. Kassas, V. Ghadiok, and T. Humphreys, "Adaptive estimation of signals of opportunity," in *Proc. ION GNSS Conf.*, Sep. 2014, pp. 1679–1689.
- [49] J. Morales and Z. Kassas, "Optimal collaborative mapping of terrestrial transmitters: Receiver placement and performance characterization," *IEEE Trans. Aerosp. Electron. Syst.*, vol. 54, no. 2, pp. 992–1007, Apr. 2018.
- [50] J. Barnes *et al.*, "Characterization of frequency stability," *IEEE Trans. Instrum. Meas.*, vol. IM-20, no. 2, pp. 105–120, May 1971.
- [51] R. Brown and P. Hwang, *Introduction to Random Signals and Applied Kalman Filtering*, 3rd ed. Hoboken, NJ, USA: Wiley, 2002.
- [52] Y. Bar-Shalom, X. Li, and T. Kirubarajan, *Estimation with Applications to Tracking and Navigation*. New York, NY, USA: Wiley, 2002.
- [53] A. Thompson, J. Moran, and G. Swenson, *Interferometry and Synthesis in Radio Astronomy*, 2nd ed. Hoboken, NJ, USA: Wiley, 2001.
- [54] I. Szottka, "Particle filtering for lane-level map-matching at road bifurcations," in *Proc. Int. IEEE Conf. Intell. Transp. Syst.*, Oct. 2013, pp. 154–159.
- [55] *Open Street Map Foundation (OSMF)*. [Online]. Available: <https://www.openstreetmap.org>
- [56] P. Bender, J. Ziegler, and C. Stiller, "Lanelets: Efficient map representation for autonomous driving," in *Proc. IEEE Intell. Vehicles Symp.*, Jun. 2014, pp. 420–425.
- [57] F. Li, P. Bonnifait, J. Ibanez-Guzman, and C. Zinoune, "Lane-level map-matching with integrity on high-definition maps," in *Proc. IEEE Intell. Veh. Symp.*, Jun. 2017, pp. 1176–1181.
- [58] A. Stone, R. Streit, T. Corwin, and K. Bell, *Bayesian Multiple Target Tracking*. Norwood, MA, USA: Artech House, 2014.
- [59] B. Ristic, S. Arulampalam, and N. Gordon, *Bayesian Multiple Target Tracking*. Boston, MA, USA: Artech House, 2004.
- [60] J. Kim, S. Yoon, S. Kang, and C. Kang, "A channel estimation technique in a DS/CDMA system with noncoherent M-ary orthogonal modulation in multipath fading channels," in *Proc. 48th Veh. Technol. Conf.*, vol. 3, May 1998, pp. 2383–2387.
- [61] T. Walter, P. Enge, J. Blanch, and B. Pervan, "Worldwide vertical guidance of aircraft based on modernized GPS and new integrity augmentations," *Proc. IEEE*, vol. 96, no. 12, pp. 1918–1935, Dec. 2008.
- [62] H. Nahavandchi and G. Joodaki, "Correlation analysis of multipath effects in GPS-code and carrier phase observations," *Surv. Rev.*, Apr. 2010. [Online]. Available: <https://doi.org/10.1179/003962610X12572516251808/>
- [63] M. Joerger, L. Gratton, B. Pervan, and C. Cohen, "Analysis of iridium-augmented GPS for floating carrier phase positioning," *NAVIGATION, J. Inst. Navigat.*, vol. 57, no. 2, pp. 137–160, 2010.
- [64] K. Shamaei and Z. Kassas, "LTE receiver design and multipath analysis for navigation in urban environments," *NAVIGATION, J. Inst. Navigat.*, vol. 65, no. 4, pp. 655–675, Dec. 2018.
- [65] P. Misra and P. Enge, *Global Positioning System: Signals, Measurements, and Performance*, 2nd ed. Lincoln, MA, USA: Ganga-Jamuna Press, 2010.
- [66] (2018). *Septentrio AsteRx-i V*. [Online]. Available: <https://www.septentrio.com/products>
- [67] K. Shamaei, J. Khalife, S. Bhattacharya, and Z. Kassas, "Computationally efficient receiver design for mitigating multipath for positioning with LTE signals," in *Proc. ION GNSS Conf.*, Sep. 2017, pp. 3751–3760.
- [68] K. Shamaei, J. Khalife, and Z. Kassas, "Comparative results for positioning with secondary synchronization signal versus cell specific reference signal in LTE systems," in *Proc. ION Int. Tech. Meeting Conf.*, Jan. 2017, pp. 1256–1268.



Mahdi Maaref received the B.S. and M.S. degrees from the University of Tehran in 2008 and 2011, respectively, and the Ph.D. degree in electrical engineering from Shahid Beheshti University, in 2016. In 2016, he joined the University of Alberta, Edmonton, Canada, as a Visiting Research Collaborator. He is currently a Post-Doctoral Research Fellow with the University of California, Irvine, and a member of the Autonomous Systems Perception Intelligent and Navigation (ASPIN) Laboratory. His research interests include autonomous ground vehicles, opportunistic perception, and autonomous integrity monitoring.



Zaher (Zak) M. Kassas (S'98–M'08–SM'11) received the B.E. degree in electrical engineering from Lebanese American University, the M.S. degree in electrical and computer engineering from The Ohio State University, and the M.S.E. degree in aerospace engineering and the Ph.D. degree in electrical and computer engineering from The University of Texas at Austin. He is currently an Assistant Professor with the University of California, Irvine, and the Director of the ASPIN Laboratory. His research interests include cyber-physical systems, estimation theory, navigation systems, autonomous vehicles, and intelligent transportation systems. He was a recipient of the National Science Foundation (NSF) Faculty Early Career Development Program (CAREER) Award in 2018 and the Office of Naval Research (ONR) Young Investigator Program (YIP) Award in 2019.